Wave dispersion analysis of three-dimensional vibroacoustic waveguides with semi-analytical isogeometric method

Fakhraddin Seyfaddini[a], H. Nguyen-Xuan[b,c], Vu-Hieu Nguyen[a,*]

[a] *MSME, CNRS UMR 8208, Univ Paris Est Creteil, Univ Gustave Eiffel, F-94010 Creteil, France*
[b] *CIRTech Institute, Ho Chi Minh City University of Technology (HUTECH), 475 Dien Bien Phu, P2, Binh Thanh, Ho Chi Minh City, Viet Nam*
[c] *Department of Architectural Engineering, Sejong University, 209 Neungdong-ro, Gwangjin-gu, Seoul, 05006, Republic of Korea*

Abstract

Material and structural non-destructive evaluations using guided-wave (GW) testing techniques rely on the knowledge of wave dispersion characteristics. When studying coupled fluid–solid waveguides having complex geometries using the semi-analytical finite element (SAFE) method, an excessive computational effort may be required, especially at high-frequency ranges. In this paper, we show the robustness of an efficient computational approach so-called the semi-analytical isogeometric analysis (SAIGA) for computing the wave dispersion in 3D anisotropic elastic waveguides coupled with acoustic fluids. This approach is based on the use of Non-Uniform Rational B-splines (NURBS) as the basis functions for the geometry representation as well as for the approximation of pressure/displacement fields. The obtained results are compared with the ones derived from using the conventional SAFE method which uses Lagrange polynomials. It is shown that for computing the dispersion of GWs, using SAIGA leads to a much faster convergence rate than using the conventional SAFE with the same shape function's order. For hollow prismatic structures immersed in fluids, using high-order NURBS (*e.g*, $p = 8$) is particularly efficient as it only requires a few elements to achieve solutions having the same precision as the ones obtained by SAFE which requires up to five times of number of DOFs. Moreover, the continuity of normal displacement at fluid–solid interfaces could be significantly improved thanks to the smoothness feature of NURBS, showing the advantage of SAIGA over SAFE in the evaluation of the shape modes of GWs in coupled fluid–solid systems.
© 2021 Elsevier B.V. All rights reserved.

Keywords: Immersed waveguides; Guided waves; Dispersion curve; Isogeometric analysis; NURBS basis; Semi analytical finite element (SAFE)

1. Introduction

Guided-wave (GW) technology, which is based on the analysis of the behavior of waves propagating along surfaces or interfaces, is widely known as a robust technique and an economical way for fast non-destructive evaluation of structures [1]. Among the wide variety of applications, one may cite the near-surface geophysics and geotechnical site characterization [2], the damage detection in composite materials [3], the characterization of fluid loaded structures [4], or more recently the ultrasonic imaging of biological tissues [5–7].

---

* Corresponding author.
   E-mail address: vu-hieu.nguyen@u-pec.fr (V.-H. Nguyen).

Due to the presence of interfaces and/or free surfaces, the waves guided along the structure have dispersive behavior, in which the phase velocity and attenuation vary with the frequency content of the wave packages. The dispersion of guided waves has been shown to strongly depend on the geometry of the structures, on the heterogeneity of material properties as well as the existence of surrounding media (most commonly fluid). Knowing the dispersion characteristics of guided waves, one may perform inversion problems to identify the geometrical and mechanical properties of the structure. Basically, the inversion procedure is performed by minimizing the error between the dispersion curves obtained from experiments and modeling [1]. Therefore, the development of low-cost and accurate computational methods for evaluating the wave dispersion is very important to enhance GW-based non-destructive techniques.

One of the most common models for studying the GWs is the cases where the medium could be assumed to be homogeneous along one (or two) directions. In these cases, the analytical methods were usually used for computing the dispersion curves, due to their efficiency in solving wave equations, especially in waveguides with simple cross-section geometry such as plates or cylinders [1]. When the section is not homogeneous but consists of multilayer materials (*i.e* the variation of properties are piecewise constant functions), the analytical solutions may also be derived by using *e.g* the transfer matrix method or the global matrix method [1]. The analytical methods have also been used to consider functionally-graded waveguides [8].

The limitations of analytical models can be circumvented by a more versatile numerical approach so-called semi-analytical finite element (SAFE) which has become popular in recent decades [9–12]. The idea of SAFE method is to assume a harmonic form of the solution in one (or two) direction and employ finite element discretization in the cross-section of the considered waveguide. In many circumstances, the considered waveguide is coupled with one or several fluid media, and we must deal with a vibroacoustic problem. While the displacement-based equation is applied in the elastic solid, the fluid may also be modeled as an elastic material with very weak shear modulus [13], or by an acoustic fluid for which the pressure-based equation is employed [14–16]. Using the elastic model employs the displacement-based equations for the fluid, which are easier to be implemented in the SAFE formulation, but it may cause spurious modes due to the zero shear modulus. Using pressure-based equations is better for describing the acoustic fluid, but continuity conditions need to be introduced between the pressure field (of the fluid) and the displacement field (of the solid) at the fluid–solid interfaces. Astaneh et al. [17,18] presented a CFEM for fluid coupled waveguides with cross-section which uses linear midpoint-integrated finite elements with specially designed set of complex-valued lengths. The proposed method has fast convergent, but only simple geometry could be considered. Zuo et al. in [16] developed SAFE formulation derived from pressure–displacement equations for considering 3D waveguides coupled with a fluid. Basically, the proposed approach is quite general and can be applied for solving any cases with arbitrary cross-section geometries. However, in practice for studying the guided waves in structures with complex cross-section geometry, a significant mesh refinement may need to be required to obtain the converged solutions, especially at high frequencies because of several reasons. First, for considering complex interfaces defined by high-gradient curves, the mesh using conventional Lagrangian finite elements needs to be extensively refined; second, as the equations in the fluid are written in terms of the pressure, the continuity conditions of normal displacement at the fluid–solid interface may not be numerically achieved due to the numerical errors of the differentiation approximation. The mesh refinement leads to larger complex-valued eigenvalue problems, causing a significant increase in computational cost.

Based on recent innovations, we propose to employ the isogeometric concept instead of conventional finite element-based discretization in the context of SAFE analysis. The isogeometric analysis employs the Computer Aided Design (CAD) concept of Non-uniform Rational B-splines (NURBS) tool to represent not only the complex geometries but also to construct approximations for finite element analysis [19–21]. In the context of the wave propagation problem, the use of NURBS basis functions, yields more accurate solutions compared to the conventional finite element analysis (FEA) using the same number of degrees of freedom [22–25]. For the simulation of GWs in elastic plates, Willberg et al. [26] compared several higher-order finite element schemes and their convergence when studying the first Lamb modes at low frequencies. In the context of GW's dispersion study, the NURBS basis functions were employed by Gravenkamp et al. [27] in the scaled boundary finite element method for the dispersion analysis of homogeneous 3D solid waveguides with arbitrary cross-section. Liu et al. [28] also applied IGA to numerical investigation of dispersive behavior of waves in helical thread waveguides. In these studies, the advantage of using IGA for the simulation of GWs in complex geometry structures has been studied. However, the presence of fluids has not been considered. Recently, by comparing with the Lagrange based approach for the

computation of dispersion curves in 2D plates (with 1D discretization) coupled with fluids, we have shown that NURBS based approach allows to improve significantly the precision and reduce the computational cost, especially at high-frequency ranges [29].

In summary, although the conventional SAFE approach has been applied widely for guided-wave analysis, the coupling between 3D prismatic solid and fluid has been much less investigated. Furthermore, to our knowledge, when using isogeometric analysis in SAFE context, most of existed works only considered simple geometries (*e.g* rectangular section) and without fluid coupling. In this work, a semi-analytical isogeometric formulation (SAIGA) was proposed for analyzing the wave dispersion in arbitrary cross-section structures immersed in fluids. To do so, the NURBS basis functions were used within the SAFE formulation established for an anisotropic elastic domain coupled with acoustic fluids in the frequency–wavenumber domain. It is expected that using high-degree NURBS basis functions could significantly improve the accuracy of the numerical solutions of the wave dispersion with a significant reduction of computational cost. The convergence analysis was carefully performed for several cases including an empty/fluid-filled cylinder and an arbitrary cross-section waveguide, which represent a typical cortical long bone geometry, in order to find optimal NURBS order for these cases. We were particularly interested in studying the continuities of stress and displacement at solid–fluid interfaces, which are important for the evaluation of the mode excitability, computed by the proposed NURBS-based analysis.

To the best of the authors knowledge, the NURBS-based modeling guided waves in 3D coupling solid–fluid structures has not been investigated in the literature. It is worth to notice that the term "semi-analytical isogeometric analysis" has also been used in the literature but in different contexts. For example, in the so-called IGA-SBFEM method [27], the IGA was used for computing the coefficient matrices of SBFEM (Scaled Boundary Finite Element Method). In [30], the W-IGA (Wave Isogeometric Analysis) method was used for the simulation wave propagation in periodic media, in which the IGA can be used for dealing with cell problems derived from Floquet–Bloch theory . In [31], a "semi-analytical isogeometric analysis" approach named as SIGA, was used for studying two-dimensional Rayleigh waves in layered composite piezoelectric structures. However, the term SIGA also widely stands for the so-called Stochastic Isogeometric Analysis and hence, we would like to not use this term to avoid confusion.

The paper is organized as follows. Section 2 describes the governing equations for three-dimensional waveguides coupled with fluid. After introducing the concept of isogeometric analysis and NURBS basis functions, Section 3 formulates the SAIGA method. Section 4 subsequently carries out the numerical dispersion analysis through several numerical examples including the free waveguide, the waveguides coupled with interior and/or exterior fluids. The convergence analysis of the phase velocities will be studied for these cases. The mode shapes and their continuities will be carefully investigated for each case. Section 5 ends with some conclusions and perspectives.

2. Problem formulation

2.1. Governing equation

Geometry description. The geometry of an immersed waveguides with arbitrary cross-section is shown in Fig. 1. The structure is described in the Cartesian coordinate system with an orthogonal basis $(\mathbf{e}_1, \mathbf{e}_2, \mathbf{e}_3)$ and the position vector $\mathbf{x} = (x_1, x_2, x_3)$. The cross section of the solid is constant along $\mathbf{e}_3$. The surfaces of the solid body may be free or loaded by two inner and outer fluids (Ω_1^f and Ω_2^f as shown in Fig. 1). The domains occupied by the solid body and the fluids are denoted by $\Omega^s = \{(x_1, x_2, x_3) | x_3 \in [-\infty, +\infty], (x_1, x_2) \in \bar{\Omega}^s\}$, $\Omega_1^f = \{(x_1, x_2, x_3) | x_3 \in [-\infty, +\infty], (x_1, x_2) \in \bar{\Omega}_1^f\}$ and $\Omega_2^f = \{(x_1, x_2, x_3) | x_3 \in [-\infty, +\infty], (x_1, x_2) \in \bar{\Omega}_2^f\}$, where $\bar{\Omega}^s$, $\bar{\Omega}_1^f$ and $\bar{\Omega}_2^f$ are the cross-section of the solid and two fluid domains. The interfaces between Ω^s and Ω_α^f ($\alpha = \{1, 2\}$) are denoted by Γ_α^{sf} ($\alpha = \{1, 2\}$). As the cross sections are unchanged along $\mathbf{e}_3$, the outward directed, normal vectors of Ω^s at Γ_α^{sf} are always perpendicular to $\mathbf{e}_3$ and may be represented by $\mathbf{n}^s = \{n_1, n_2, 0\}^T$. In what follows, the symbol $\partial_i(\star)$ ($i = 1, 2, 3$) stands for the partial derivative of $(\star)$ with respect to x_i.

Dynamic equations in the solid layer. In the solid domain Ω^s, the infinitesimal displacement vector at a point $\mathbf{x}$ and at time t is denoted by $\mathbf{u}^s(\mathbf{x}, t) = \{u_1, u_2, u_3\}^T$. For the purpose of convenience, here we use the Voigt notation which represents the stress and strain under the vectorial form as follows $\mathbf{s}(\mathbf{x}, t) = \{\sigma_{11}, \sigma_{22}, \sigma_{33}, \sigma_{23}, \sigma_{13}, \sigma_{12}\}^T$ and $\mathbf{e}(\mathbf{x}, t) = \{\varepsilon_{11}, \varepsilon_{22}, \varepsilon_{33}, 2\varepsilon_{23}, 2\varepsilon_{13}, 2\varepsilon_{12}\}^T$, respectively. As $\varepsilon_{ij} = \frac{1}{2}(\partial_i u_j + \partial_j u_i)$, the strain vector $\mathbf{e}$ can be expressed by: $\mathbf{e} = \mathbb{L}\mathbf{u}^s$, where $\mathbb{L} = \mathbf{L}_1\partial_1 + \mathbf{L}_2\partial_2 + \mathbf{L}_3\partial_3$. The matrices $\mathbf{L}_1$, $\mathbf{L}_2$ and $\mathbf{L}_3$ are 3×2 matrices of which the nonzero entries are: $\mathbf{L}_1(1, 1) = \mathbf{L}_1(5, 3) = \mathbf{L}_1(6, 2) = 1$, $\mathbf{L}_2(2, 2) = \mathbf{L}_2(4, 3) = \mathbf{L}_2(6, 1) = 1$ and $\mathbf{L}_3(3, 3) = \mathbf{L}_3(4, 2) = \mathbf{L}_3(5, 1) = 1$, respectively.
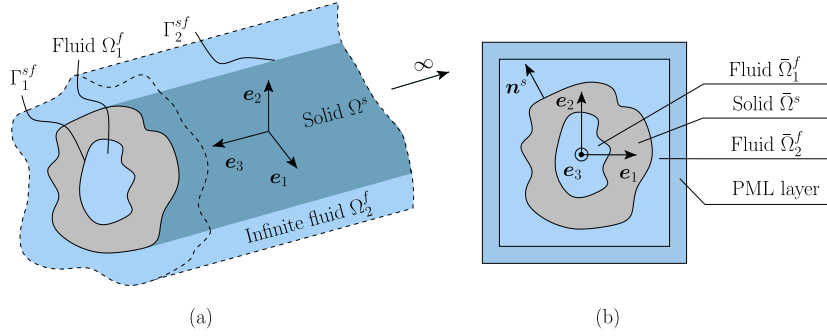
Fig. 1. Schematic of (a) fluid-filled solid waveguide with arbitrary cross-section immersed in an infinite fluid (b) cross-section with the PML layer.

The balance equations of linear momentum at a point $x \in \Omega^s$ and the linear elastic constitutive law read

$$\rho \ddot{\boldsymbol{u}}^s - \mathbb{L}^T \boldsymbol{s} = 0 , \tag{1}$$

$$\boldsymbol{s} = \mathbf{C}\boldsymbol{e} , \tag{2}$$

where ρ is the mass density, $\mathbf{C}_{6 \times 6}$ is the matrix containing the components of the anisotropic elasticity tensor. In this problem, the structure is assumed to be homogeneous along the longitudinal direction $\mathbf{e}_3$ but it could be heterogeneous in the section $\bar{\Omega}^s$, *i.e.* $\rho = \rho(x_1, x_2)$ and $\mathbf{C} = \mathbf{C}(x_1, x_2)$.

Wave equations in the fluids. In the fluid domains Ω_α^f ($\alpha = 1, 2$), the linearized wave equations can be expressed as

$$\rho_\alpha^f \ddot{p}_\alpha - K_\alpha^f \nabla^2 p_\alpha = 0 , \tag{3}$$

where p_α are the acoustic pressure fields in Ω_α^f, K_α^f and ρ_α^f are the bulk modulus at rest and the mass density at rest of the Ω_α^f, respectively; $\nabla^2(\star)$ is the Laplace operator. The wave celerity in Ω_α^f can be defined as $c_\alpha^f = \sqrt{K_\alpha^f / \rho_\alpha^f}$.

Boundary and interface conditions. The boundary conditions of this system (Eqs. (1) & (3)) consist of the continuity conditions of the traction and of the normal displacement at the solid–fluid interfaces $\bar{\Gamma}_\alpha^{sf}$ ($\alpha = \{1, 2\}$), and the radiation condition at infinity, i.e.

$$\left.\begin{array}{r} \boldsymbol{t} = -p_\alpha \boldsymbol{n}^s \\ \boldsymbol{u}^s \cdot \boldsymbol{n}^s = \boldsymbol{u}_\alpha^f \cdot \mathbf{n}^s \end{array}\right\} \quad \forall \boldsymbol{x} \in \bar{\Gamma}_\alpha^{sf} , \tag{4}$$

$$p_\alpha \to 0 \qquad \text{when } |\boldsymbol{x}| \to \infty , \tag{5}$$

where $\boldsymbol{n}^s$ is the outward unit vector at the interfaces (Fig. 1), which is opposed to the one of the fluid domain: $\boldsymbol{n}^s = -\boldsymbol{n}^f$. It is worth noting that $\boldsymbol{t} = \boldsymbol{\sigma} \cdot \boldsymbol{n}^s = (n_1 \mathbf{L}_1^T + n_2 \mathbf{L}_2^T)\boldsymbol{s}$ and the fluid displacement may be calculated from the pressure field by using the Euler's equation:

$$\rho_\alpha^f \ddot{\boldsymbol{u}}_\alpha^f + \nabla p_\alpha = 0. \tag{6}$$

2.2. Perfectly Matched Layer (PML)

In order to introduce the behavior of the infinite exterior fluid domain, we used the perfectly matched layers (PML) in the cross-section plane, following the procedures proposed in [9,16]. From a mathematical point of view, the PML can be considered as a result of a mapping into complex coordinates, where the solutions of wave equations decay exponentially [32]. Therefore, the infinite medium can be truncated into a finite domain as shown in Fig. 1. The new stretched coordinates $\tilde{x}_1(x_1)$, $\tilde{x}_2(x_2)$ in the waveguide are defined as

$$\tilde{x}_1(x_1) = \int_0^{x_1} \gamma_1(x_1) dx_1, \qquad \tilde{x}_2(x_2) = \int_0^{x_2} \gamma_2(x_2) dx_2, \tag{7}$$

where $\gamma_1(x_1)$ and $\gamma_2(x_2)$ are called PML functions, which satisfy:

$$\gamma_j(x_j) = 1 \text{ for } |x_j| \leq d_j \text{ and } \text{Im}\{\gamma_j(x_j)\} > 0 \text{ for } |x_j| > d_j, \quad \text{for } j = \{1, 2\}, \tag{8}$$

On the exterior boundary of the PML, the boundary condition can be arbitrarily chosen (Dirichlet or Neumann type). The absorption efficiency of leaky waves in the PML strongly depends on the choice of the PML function (γ_1, γ_2), the position of the interfaces (d_1, d_2) and the thickness ($h_1^{\text{pml}}, h_2^{\text{pml}}$) in the $\mathbf{e}_1$ and $\mathbf{e}_2$ directions, respectively. There are a number of variants to choose for the γ_1 and γ_2 functions. For this study, a continuous parabolic function for both the real and imaginary parts of the PML function, which has been demonstrated to be efficient in the frequency domain [9,16], was used:

$$\gamma_j(x_j) = \begin{cases} 1 & \text{if } |x_j| \leq d_j, \\ 1 + \hat{\gamma}_j \left(\frac{|x_i| - d_j}{h_j^{\text{pml}}} \right)^2 & \text{if } |x_j| > d_j, \end{cases} \quad \text{for } j = \{1, 2\}, \tag{9}$$

where $\hat{\gamma}_j = a_j + ib_j$ quantify the PML absorption and will be given explicitly in each case study. As leaky waves grow exponentially in the transverse directions, placing the PML close to the waveguide can reduce the effect of the exponential growth of the leaky modes. In order to estimate the length of the PML, a simplified 2D plane wave propagation model can be used to approximately predict the length of the PML:

$$h_j^{\text{pml}} \geq \frac{6.9}{k_{\text{leak}} b_j}, \quad \text{for } j = \{1, 2\}, \tag{10}$$

where k_{leak} represents the wavenumber of the longitudinal wave in the fluid. When the PML function is given, b_j can be determined as $\text{Im}(\hat{\gamma}_j)$. The length of the PML can be obtained by calculating the smallest wavenumber in the frequency range of interest [16].

It is worth noting that in the context of the SAFE analysis, several techniques have been proposed for representing the radial boundary condition in semi-infinite domains. For example, in [15], the coupled boundary element and finite element method (referred as 2.5D FEM–BEM) has been used. However, this method leads to a nonlinear eigenvalue problem that requires an expensive solution strategy. In [33], an iterative procedure was proposed to solve the nonlinear eigenvalue problem derived from exact radiation condition. For the case of an immersed plate, the nonlinear eigenvalue problem with exact radiation condition was transformed into a cubic polynomial eigenvalue problem using a change of variables [34]. However, its extension to 3D cases is not trivial. Although using a PML within SAFE formulation requires a supplement layer with a thickness about two wavelengths, it has some attractive advantages because (i) it allows us to avoid the nonlinear term in the exact radiation condition and thus the final eigenvalue problem established for the coupled fluid–solid system still has the quadratic polynomial form, which may efficiently be solved (as it will be shown in Section 3); (ii) the implementation of PMLs in the SAFE formulation is straightforward and requires very little modifications.

2.3. Weak formulation in the frequency–wavenumber domain

We look for the solution of harmonic waves propagating along the axial direction ($\mathbf{e}_3$), which may be expressed by the following form

$$\boldsymbol{u}^s(x_1, x_2, x_3, t) = \tilde{\boldsymbol{u}}^s(x_1, x_2)e^{i(k_3 x_3 - \omega t)}, \tag{11a}$$

$$p_\alpha(x_1, x_2, x_3, t) = \tilde{p}_\alpha(x_1, x_2)e^{i(k_3 x_3 - \omega t)}, \tag{11b}$$

where $i^2 = -1$; $\omega \in \mathbb{R}$ is the angular frequency; k_3 is the wavenumber in the $\mathbf{e}_3$-direction; the vector $\tilde{\boldsymbol{u}}^s(x_1, x_2) = (\tilde{u}_1, \tilde{u}_2, \tilde{u}_3)^T$ and $\tilde{p}_\alpha(x_1, x_2) = \tilde{p}_\alpha$ are the amplitudes of the displacement vector in the $\bar{\Omega}^s$ and of the pressures in $\bar{\Omega}_\alpha^f$, respectively. By applying harmonic forms (Eqs. (11a), (11b)), the problem presented in Section 2.1 can be transformed to a 2D system of equations with respect only to x_1 and x_2 (see Appendix A for the detailed development).

Upon integrating Eqs. (A.3)–(A.4) against test function $\delta\tilde{\boldsymbol{u}}^s$ and $\delta\tilde{p}_\alpha$, respectively, then applying the Gauss theorem and taking into account the interface conditions (A.5), the weak formulation of the boundary value problem

in the solid layer $\bar{\Omega}^s$ and in the fluid domain $\bar{\Omega}_\alpha^f$ ($\alpha = \{1, 2\}$) may be derived as in [35]:

$$-\omega^2 \int_{\bar{\Omega}^s} \delta\tilde{\boldsymbol{u}}^s \cdot \rho\tilde{\boldsymbol{u}}^s d\bar{\Omega}^s + \int_{\bar{\Omega}} \left(\mathbf{L}_1\partial_1 + \mathbf{L}_2\partial_2 - \mathrm{i}k_3\mathbf{L}_3\right)\delta\tilde{\boldsymbol{u}}^s \cdot \left(\mathbf{C}(\mathbf{L}_1 + \mathbf{L}_2\partial_2 + \mathrm{i}k_3\mathbf{L}_3)\tilde{\boldsymbol{u}}^s\right)d\bar{\Omega}^s$$

$$+ \int_{\bar{\Gamma}_\alpha^{sf}} \delta\tilde{\boldsymbol{u}}^s \cdot \left(\tilde{p}_\alpha\boldsymbol{n}^s\right)d\bar{\Gamma}_\alpha^{sf} = 0 , \quad \forall \delta\tilde{\boldsymbol{u}}^s \in \mathcal{C}^{ad}. \tag{12a}$$

$$-\omega^2 \int_{\bar{\Omega}_\alpha^f} \delta\tilde{p}_\alpha^* \rho_\alpha^f \tilde{p}_\alpha d\bar{\Omega}_\alpha^f - \omega^2 \int_{\bar{\Gamma}_\alpha^{sf}} \delta\tilde{p}_\alpha^* \rho_\alpha^f K_\alpha^f \tilde{\boldsymbol{u}}^s \cdot \boldsymbol{n}^s d\bar{\Gamma}_\alpha^{sf} + k_3^2 \int_{\bar{\Omega}_\alpha^f} \delta\tilde{p}_\alpha K_\alpha^f \tilde{p}_\alpha d\bar{\Omega}_\alpha^f$$

$$+ \int_{\bar{\Omega}_\alpha^f} \left((\partial_1\delta\tilde{p}_\alpha)^* K_\alpha^f \partial_1 \tilde{p}_\alpha + (\partial_2\delta\tilde{p}_\alpha)^* K_\alpha^f \partial_2 \tilde{p}_\alpha\right)d\bar{\Omega}_\alpha^f = 0 , \quad \forall \delta\tilde{p}_\alpha \in \mathcal{C}^{ad}. \tag{12b}$$

3. NURBS-based isogeometric approximation

The formulation presented in Eqs. (12a)–(12b) is valid irrespective of the numerical discretization employed in the cross-section. In the framework of conventional SAFE, the Lagrange polynomials are used to discretized these equations. The main drawback of this approach, which is also called a SAFE method, is the fact that discretization should be fine enough to achieve the required accuracy. The consequence of fine discretization is a significant increase in computational cost. Furthermore, the Lagrange PML functions give a non-smoothness profile across the PML interfaces, which leads to imperfect absorption of the leaky modes. We propose to use a different technique for computational efficiency. The idea is based on the NURBS-based isogeometric analysis allowing the use of globally C^k-continuous basis functions, with $k \leq p - 1$, p being the polynomial degree. In this section, we briefly recall the concept of isogeometric analysis with the main focus on the B-spline and NURBS basis functions, their properties, their use for the geometrical representation as well as incorporating the interface with the C^0-continuity. For a more detailed review of these topics, we refer the interested reader to [36,37].

3.1. Geometrical representation

NURBS are piecewise rational functions of degree p that are connected in so-called knots. Let $\Xi = \{\xi_1, \xi_2, \xi_3, \ldots, \xi_{n+p+1}\}$ and $H = \{\eta_1, \eta_2, \eta_3, \ldots, \eta_{m+p+1}\}$ be the knot vectors in the bi-dimensional parametric domain $\hat{\Omega}$, each consisting of nondecreasing real numbers ξ_i and η_i, respectively. The bivariate NURBS basis functions are defined by:

$$R_{ij}^{p,q}(\xi, \eta) = \frac{N_{i,p}(\xi)N_{j,q}(\eta)w_{ij}}{\sum_{k=1}^n \sum_{\ell=1}^m N_{k,p}(\xi)N_{\ell,q}(\eta)w_{k\ell}}, \tag{13}$$

where $N_{i,p}$ denotes the ith B-spline basis function of p-degree, $w_{k\ell} \in \mathbb{R}$ is the weight values and n, m are the numbers of basis functions used to construct the B-spline curve in each dimension. By using the well-known Cox–de Boor formula, the B-spline basis functions are defined recursively as:

$$N_{i,0}(\xi) = \begin{cases} 1 & \text{if } \xi_i < \xi < \xi_{i+1}, \\ 0 & \text{otherwise}, \end{cases} \tag{14a}$$

$$N_{i,p}(\xi) = \frac{\xi - \xi_i}{\xi_{i+p} - \xi_i}N_{i,p-1}(\xi) + \frac{\xi_{i+p+1} - \xi}{\xi_{i+p+1} - \xi_{i+1}}N_{i+1,p-1}(\xi). \tag{14b}$$

Note that the quotient 0/0 is assumed to be zero. By introducing a set of control points $\mathbf{P}_{ij} \in \mathbb{R}^2$, the NURBS surfaces are constructed by:

$$\boldsymbol{S}(\xi, \eta) = \sum_{i=1}^n \sum_{j=1}^m R_{ij}^{p,q}(\xi, \eta)\mathbf{P}_{ij} . \tag{15}$$

3.2. Solution approximation

Let v^h denote the approximation of a function $v(x_1, x_2)$ defined in the physical domain Ω. According to the isogeometric concept [37], the function v^h may be given by a composition between a function $\hat{v}^h$, defined in the

parametric domain $\hat{\Omega}$, with the inverse of geometrical mapping: $v^h = \hat{v}^h \circ \mathbf{x}^{-1}$. The function $\hat{v}^h$ is built over the parametric domain by:

$$\hat{v}^h(\xi, \eta) = \sum_{i=1}^{n} \sum_{j=1}^{m} R_{ij}^{p,q}(\xi, \eta) V_{ij} \,, \tag{16}$$

where the coefficients $V_{ij} \in \mathbb{C}$ are the corresponding control variables (values at the control points $\mathbf{P}_{ij}$). The properties of the function $\hat{v}^h$ follow those of the NURBS basis functions.

In this study, by using Galerkin's method, the same approximations are applied for both functions $\tilde{\mathbf{u}}^h$ and $\delta\tilde{\mathbf{u}}^h$ (as well as for $\tilde{p}_\alpha^h$ and $\delta\tilde{p}_\alpha^h$) on each patch:

$$\tilde{\mathbf{u}}^h = \mathbf{R}^u \mathbf{U}, \quad \delta\tilde{\mathbf{u}}^h = \mathbf{R}^u \delta\mathbf{U}, \tag{17a}$$

$$\tilde{p}_\alpha^h = \mathbf{R}_\alpha^p \mathbf{P}_\alpha, \quad \delta\tilde{p}_\alpha^h = \mathbf{R}_\alpha^p \delta\mathbf{P}_\alpha, \tag{17b}$$

where $\mathbf{R}^u$, $\mathbf{R}^p$ are the interpolation matrix containing the NURBS basis functions (Eq. (13)); $\mathbf{U}$ and $\delta\mathbf{U}$ are the vectors of control displacements; $\mathbf{P}_\alpha$ and $\delta\mathbf{P}_\alpha$ are the vectors of control pressures. By substituting the approximations (Eqs. (17a)–(17b)) into the weak formulations (Eqs. (12a)–(12b)), then assembling the elementary matrices, one obtains

$$(-\omega^2 \mathbf{M} + \mathbf{K}_0 + ik_3 \mathbf{K}_1 + k_3^2 \mathbf{K}_2)\mathbf{V} = \mathbf{0} \,, \tag{18}$$

where $\mathbf{V} = (\mathbf{P}_1, \mathbf{U}, \mathbf{P}_2)^T$ containing the global eigenvectors of pressure ($\mathbf{P}_1$, $\mathbf{P}_2$) and of displacement ($\mathbf{U}$); the global matrices $\mathbf{M}$, $\mathbf{K}_0$, $\mathbf{K}_1$, $\mathbf{K}_2$ are defined by:

$$\mathbf{M} = \begin{bmatrix} \mathbf{M}^{f_1} & \mathbf{M}^{f_1 s} & \mathbf{0} \\ \mathbf{0} & \mathbf{M}^s & \mathbf{0} \\ \mathbf{0} & \mathbf{M}^{f_2 s} & \mathbf{M}^{f_2} \end{bmatrix}, \quad \mathbf{K}_0 = \begin{bmatrix} \mathbf{K}_0^{f_1} & \mathbf{0} & \mathbf{0} \\ \mathbf{K}^{s f_1} & \mathbf{K}_0^s & \mathbf{K}^{s f_2} \\ \mathbf{0} & \mathbf{0} & \mathbf{K}_0^{f_2} \end{bmatrix}, \tag{19a}$$

$$\mathbf{K}_1 = \begin{bmatrix} \mathbf{0} & \mathbf{0} & \mathbf{0} \\ \mathbf{0} & \mathbf{K}_1^s & \mathbf{0} \\ \mathbf{0} & \mathbf{0} & \mathbf{0} \end{bmatrix}, \quad \mathbf{K}_2 = \begin{bmatrix} \mathbf{K}_2^{f_1} & \mathbf{0} & \mathbf{0} \\ \mathbf{0} & \mathbf{K}_2^s & \mathbf{0} \\ \mathbf{0} & \mathbf{0} & \mathbf{K}_2^{f_2} \end{bmatrix}, \tag{19b}$$

in which, the sub-matrices are determined from the assembling of corresponding elementary matrices in solid and fluid domains: the sub-matrices (with superscript ^{s}) representing the behavior of the solid domain are defined by:

$$\mathbf{M}^s = \bigcup_e \int_{\bar{\Omega}^{s(e)}} (\mathbf{R}^u)^T \rho \mathbf{R}^u d\bar{\Omega}^s, \tag{20a}$$

$$\mathbf{K}_0^s = \bigcup_e \int_{\bar{\Omega}^{s(e)}} \left(\partial_i (\mathbf{R}^u)^T \mathbf{A}_{ij} \partial_j \mathbf{R}^u \right) d\bar{\Omega}^s, \quad \text{for } i, j = \{1, 2\}, \tag{20b}$$

$$\mathbf{K}_1^s = \bigcup_e \int_{\bar{\Omega}^{s(e)}} \left(-(\mathbf{R}^u)^T \mathbf{A}_{3i} \partial_i \mathbf{R} + \partial_i (\mathbf{R}^u)^T \mathbf{A}_{i3} \mathbf{R}^u \right) d\bar{\Omega}^s, \quad \text{for } i = \{1, 2\}, \tag{20c}$$

$$\mathbf{K}_2^s = \bigcup_e \int_{\bar{\Omega}^{s(e)}} (\mathbf{R}^u)^T \mathbf{A}_{33} \mathbf{R}^u d\bar{\Omega}^s, \tag{20d}$$

the sub-matrices (with superscript ^{f}) representing the behavior of the fluid domains are defined by

$$\mathbf{M}^{f_\alpha} = \bigcup_e \int_{\bar{\Omega}_\alpha^f} (\mathbf{R}^p)^T \rho_\alpha^f \gamma_1 \gamma_2 \mathbf{R}^p d\bar{\Omega}_\alpha^f, \tag{21a}$$

$$\mathbf{K}_0^{f_\alpha} = \bigcup_e \int_{\bar{\Omega}_\alpha^f} \partial_2 (\mathbf{R}^p)^T K_\alpha^f \gamma_1 \gamma_2 \partial_2 \mathbf{R}^p d\bar{\Omega}_\alpha^f, \tag{21b}$$

$$\mathbf{K}_2^{f_\alpha} = \bigcup_e \int_{\bar{\Omega}_\alpha^f} (\mathbf{R}^p)^T K_\alpha^f \gamma_1 \gamma_2 \mathbf{R}^p d\bar{\Omega}_\alpha^f, \tag{21c}$$

and sub-matrices $\mathbf{M}^{f\alpha s}$ and $\mathbf{K}^{sf\alpha}$ representing the coupling operator at fluid–solid interfaces:

$$\mathbf{M}^{f\alpha s} = \int_{\bar{\Gamma}_\alpha^{sf}} (\mathbf{R}^p)^T \rho_\alpha^f K_\alpha^f \mathbf{R}^u d\bar{\Gamma}_\alpha^{sf}, \tag{22a}$$

$$\mathbf{K}^{sf\alpha} = \int_{\bar{\Gamma}_\alpha^{sf}} (\mathbf{R}^u)^T \mathbf{R}^p d\bar{\Gamma}_\alpha^{sf}. \tag{22b}$$

The matrices $\mathbf{M}$, $\mathbf{K}_0$, $\mathbf{K}_1$, $\mathbf{K}_2$ are computed by using two-dimensional Gauss–Legendre quadrature formula with $r = p+1$ quadrature nodes per element along each parametric direction which has been shown to be efficient [38]. Due to the fact that $\mathbf{A}_{\alpha\beta} = \mathbf{A}_{\beta\alpha}^T$, it can be shown that $\mathbf{M}$, $\mathbf{K}_0$, $\mathbf{K}_2$ are symmetric while the matrix $\mathbf{K}_1$ is anti-symmetric. In this paper, where the material is assumed to be elastic, these matrices are real and constant with respect to ω and k_3. In the case where viscoelastic materials are considered, the elasticity tensor $\mathbf{C}$ can be by replaced by a complex tensor $\mathbf{C}(\omega)$, which depends on the frequency. Then same formulations (Eqs. (20a)–(22b)) can be used for taking into account viscosity effects. In that case, the matrices $\mathbf{K}_0$, $\mathbf{K}_1$, $\mathbf{K}_2$ will depend on ω, but still independent to k_3.

It is worth to note that the quadratic eigenvalue equation (18) can be converted into a generalized linear eigenvalue problem for the media possessing orthorhombic symmetry (more details can be found in [18]).

3.3. Dispersion analysis

The system of characteristic equations (18) is an eigenvalue problem which is used to determine the relationship between the pulsation ω and the wavenumber k_3. By noting that all global matrices ($\mathbf{M}$, $\mathbf{K}_0$, $\mathbf{K}_1$, $\mathbf{K}_2$) do not depend on k_3, Eq. (18) is a quadratic eigenvalue problem with respect to k_3 and could be solved by reformulating it under following linearized eigenvalue problem:

$$\left(\begin{bmatrix} \mathbf{0} & -\omega^2\mathbf{M} + \mathbf{K}_0 \\ -\omega^2\mathbf{M} + \mathbf{K}_0 & i\mathbf{K}_1 \end{bmatrix} - k_3 \begin{bmatrix} -\omega^2\mathbf{M} + \mathbf{K}_0 & \mathbf{0} \\ \mathbf{0} & -\mathbf{K}_2 \end{bmatrix} \right) \begin{pmatrix} \mathbf{V} \\ k_3\mathbf{V} \end{pmatrix} = \mathbf{0} . \tag{23}$$

For each value of the angular frequency ω, solving Eq. (23) allows us to determine the eigenvalues k_3 and their associated eigenvectors (also called by wave structures), $\mathbf{V}(\omega, k_3)$ of guided modes. The frequency-dependent phase velocity (C_{ph}) and the attenuation (att) of a guided mode are given by:

$$C_{\mathrm{ph}} = \frac{\omega}{\mathsf{Re}(k_3)} \; [\mathrm{m \; s^{-1}}], \quad \mathrm{att} = \mathsf{Im}(k_3) \; [\mathrm{Np \; m^{-1}}] , \tag{24}$$

where $\mathsf{Re}()$ and $\mathsf{Im}()$ denote the real and imaginary parts of a complex function.

Three kinds of modes can be found for the immersed waveguides: the trapped mode, the leaky mode and the radiation mode. As the name indicates, trapped modes propagate in the waveguide with energy concentrating in the waveguide. Leaky modes propagate along the waveguide with some energy leaking into the surrounding fluid. Radiation modes resonate mainly in the fluid domain, and they are of less interest in practical applications [39]. For the studies presented in this paper, the following filtering condition is applied in post-processing to identify and remove the radiation modes: $\frac{|E_k^f|}{|E_k|} > \eta$, where E_k^f and E_k are the kinetic energy of the fluid domain and the total kinetic energy of all domains, respectively; η is a user-defined parameter, identifying the criterion of the model and depends on PML parameters (in this paper, a value $\eta = 0.98$ was used for all examples).

4. Numerical results

This section presents some numerical examples in order to validate the accuracy of the proposed SAIGA formulations for the analysis of the dispersion of guided waves in 3D elastic structures. First, a hollow cylinder in vacuum will be considered (Fig. 2(a)). Second, the wave dispersion of the waveguides coupled with fluids (inner and outer) will be studied (Fig. 2(b) and (c)). The PML is applied to absorb the leaky wave in the infinite exterior fluid. Third, the wave dispersion within a 3D waveguide with a complex section representing an anisotropic cortical bone will be analyzed (Fig. 2(d)). The validations were done by comparing the solutions obtained using the proposed SAIGA approach, by the conventional SAFE method and by analytical analysis (which only exist for the homogeneous or layered plates and cylinders). In this study, all analytical solutions were obtained by using the software DISPERSE [40] and the conventional SAFE solutions by implementing the weak formulations (Section 2.3) into the software COMSOL Multiphysics (COMSOL AB, Stockholm, Sweden), in which, the isoparametric elements
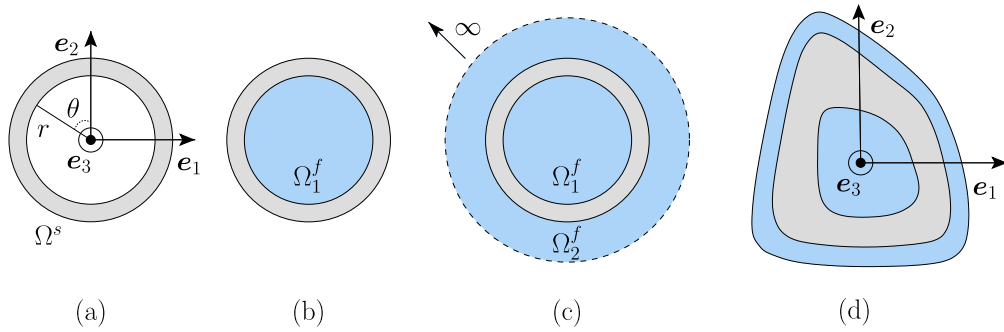
Fig. 2. Overview of the studied waveguides: (a) hollow cylinder (without fluid); (b) fluid-filled cylinder; (c) immersed fluid-filled cylinder; and (d) cortical bone with arbitrary cross-section.

were used for the discretization. In all examples, the order of basis functions in the direction $\mathbf{e}_1$ and $\mathbf{e}_2$ are assumed to be the same and denoted by p.

The convergence analysis was performed for two cases: free hollow cylinder and fluid-filled cylinder. In order to carry out a convergence analysis of the proposed method at a given frequency, we introduced a function err which is estimated as the summation of the relative errors of the numerical solutions of the first m modes:

$$\mathsf{err} = \sqrt{\sum_{i=1}^{m} \frac{(C_{\mathrm{ph}}^{i,num} - C_{\mathrm{ph}}^{i,ref})^2}{(C_{\mathrm{ph}}^{i,ref})^2}} \,, \tag{25}$$

where $C_{\mathrm{ph}}^{i,num}(f)$ is the phase velocity of ith mode at a frequency f calculated by using SAFE or SAIGA, $C_{\mathrm{ph}}^{i,ref}$ is the corresponding reference solution. For the case of a homogeneous cylinder, the reference solution can be obtained analytically by using Disperse software (homogeneous cylindrical case). When the section has irregular shapes, the analytical solution does not exist, then the reference solutions were numerically computed by using the conventional SAFE method with a very fine mesh.

4.1. Dispersion of guided-waves in a hollow cylinder

Let us first consider a free hollow cylinder, which is a well-known case and has been studied in many works using analytical or the conventional SAFE methods (see *e.g* [1]). Although the solutions of dispersed guided-waves in a free hollow cylinders were well-known, this benchmark example will allow us to validate and show the effectiveness of the proposed SAIGA method compared with the conventional SAFE method, especially for the evaluation of the phase velocities and mode shapes at the high-frequency range.

In this example, the hollow cylinder is made by 2 mm-thickness steel material with the inner radius of 5 mm (Fig. 2(a)). The isotropic elastic properties of the steel are characterized by the density $\rho = 7840$ kg m^{-3}, the longitudinal wave velocity $c_P = 5900$ m/s and the shear wave velocity $c_S = 3200$ m/s. Cubic NURBS basis functions are used for SAIGA and cubic Lagrange polynomials are used for SAFE analysis, so that the number of degrees of freedom $N_{\mathrm{dof}} = 1080$ for both numerical approaches. When employing SAIGA, four patches are used to represent the geometry of the annular section. Phase velocities are computed within a frequency range from 0 to 2 MHz.

The results of both numerical approaches are shown in Fig. 3 and are compared with the analytical solution using global matrix method. Fig. 3(a) depicts all propagating modes (of which k_3 are reals and positives) computed by SAIGA or IGA methods. Among them, three fundamental modes were interested: axisymmetric longitudinal modes $L(0, n)$, non-axisymmetric flexural modes $F(1, n)$ and torsional modes $T(0, n)$, where integer n represents the group order of a mode. The filtering criteria to select these modes are presented in Appendix B. After applying the filtering procedure to the solutions presented in Fig. 3(a), the mentioned modes may be separated as shown in Fig. 3(b). One may notice that in the dispersion curves obtained by using SAFE method, some modes are missed, namely in high frequency range. It is because when the mesh is not sufficiently fine, the fundamental modes defined by proposed criteria may not be identified due to numerical errors. On contrary, SAIGA solutions show a very well agreement with the analytical ones over entire frequency range and for all the considered modes. It means that using
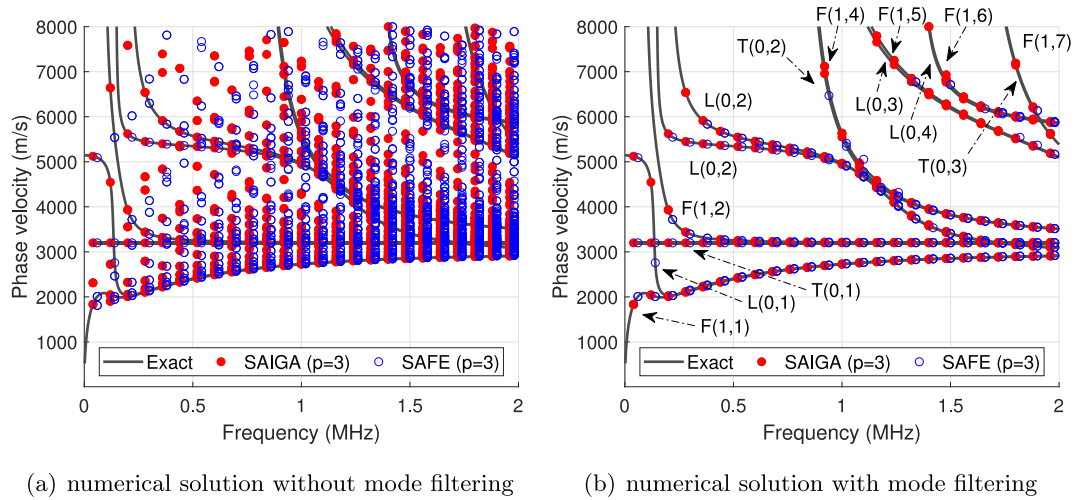
(a) numerical solution without mode filtering   (b) numerical solution with mode filtering

Fig. 3. Dispersion curves of a steel cylinder: comparison between SAIGA solution (red marker), SAFE (blue marker) and analytical solutions (gray line); both SAIGA and SAFE used $p = 3$, $N_{\text{dof}} = 1080$. (For interpretation of the references to color in this figure legend, the reader is referred to the web version of this article.)

Table 1

Case of a homogeneous hollow cylinder: error analysis of SAIGA solutions based on p-refinement (one single element per patch).

Mode	f (MHz)	$C_{\text{ph}}^{\text{Exact}}$ (m s^{-1})	err$^{\text{SAIGA}}$ ($p = 2$, $N_{\text{dof}} = 72$)	err$^{\text{SAIGA}}$ ($p = 3$, $N_{\text{dof}} = 144$)	err$^{\text{SAIGA}}$ ($p = 4$, $N_{\text{dof}} = 240$)	err$^{\text{SAIGA}}$ ($p = 6$, $N_{\text{dof}} = 504$)
L(0,1)	0.2	2027.64	0.0082	1.8020×10^{-4}	2.5573×10^{-6}	8.8473×10^{-7}
F(1,1)	0.2	2007.44	0.0156	5.4788×10^{-4}	2.3993×10^{-5}	8.5000×10^{-7}
L(0,1)	2	2910.29	0.0526	0.0241	0.0044	4.7768×10^{-5}
L(0,3)	2	5095.31	0.2002	0.0926	0.0135	1.1250×10^{-4}
L(0,4)	2	5845.90	0.1381	0.0250	0.0068	9.0413×10^{-5}
F(1,1)	2	2912.34	0.0528	0.0241	0.0044	4.7835×10^{-5}
F(1,5)	2	5103.56	0.2021	0.0938	0.0134	1.1138×10^{-4}
F(1,6)	2	5864.83	0.1392	0.0251	0.0069	9.1223×10^{-5}
F(1,7)	2	5403.87	–	–	0.0070	3.7099×10^{-5}
T(0,3)	2	5385.32	–	–	0.0068	3.5097×10^{-5}

SAIGA formulation allows to obtain better estimations not only of the eigenvalues but also of the eigenvectors of the considered system.

To quantify the accuracy of the phase velocity computed by SAIGA, we first study the p-convergence of SAIGA method at two different frequencies: $f = 0.2$ MHz and $f = 2$ MHz. To do so, the section is discretized into 4 patches (with C^0 continuity between the patches) and one single span (element) in each patch (*e.g.* the knot vectors for $p = 2$ and $p = 3$ are $\Xi = H = \{0, 0, 0, 1, 1, 1\}$ and $\Xi = H = \{0, 0, 0, 0, 1, 1, 1, 1\}$, respectively). The p-refinement is then applied in which the order of NURBS basis functions is varied: $p = 2, 3, 4, 6$. The numerical errors of the phase velocities (Eq. (25)) associated to different modes (see Fig. 3(b)) are presented in Table 1. At the low frequency $f = 0.2$ MHz, the p-convergence could be quickly achieved. For example, using the cubic function ($p = 3$) is sufficient to obtain a good estimation (with errors of order 10^{-4}) of the phase velocities of L(0,1) and F(1,1) modes. At a high frequency ($f = 2$ MHz), the errors are significant and have orders of 10^{-1} and 10^{-2} when using the quadratic and cubic NURBS basis functions, respectively. Eventually, the higher modes F(1,7) and T(0,3) cannot be identified by filtering the numerical solutions of eigenvectors. Using higher-order NURBS basis functions ($p = 4$ and $p = 6$) clearly allow to obtain much smaller errors for all modes, showing the p-convergence of NURBS-based formulations.

Table 2 presents the numerical errors of SAIGA and SAFE solutions obtained when applying the h-refinement. The basis function's order was fixed at $p = 3$ for all cases. Note that when using SAFE with a mesh of $N_{\text{dof}} = 360$, the studied modes could not be identified as the annular geometry cannot correctly be described by few quadratic

Table 2

Case of a homogeneous hollow cylinder: error analysis of SAIGA and SAFE solutions based on h-refinement with basis function's order $p = 3$.

Mode	f (MHz)	C_{ph}^{Exact} (m s^{-1})	err^{SAIGA} ($N_{dof} = 360$)	err^{SAIGA} ($N_{dof} = 504$)	err^{SAIGA} ($N_{dof} = 1080$)	err^{SAFE} ($N_{dof} = 504$)	err^{SAFE} ($N_{dof} = 1080$)
L(0,1)	0.2	2027.64	7.3118×10^{-7}	1.4290×10^{-7}	5.7945×10^{-9}	3.4599×10^{-5}	2.9142×10^{-6}
F(1,1)	0.2	2912.34	8.8493×10^{-6}	1.5434×10^{-6}	4.3057×10^{-8}	1.5836×10^{-4}	1.8420×10^{-5}
L(0,1)	2	2910.29	0.0016	3.5389×10^{-4}	1.5429×10^{-5}	0.0047	9.0892×10^{-4}
L(0,3)	2	5095.31	0.0046	7.6841×10^{-4}	1.5385×10^{-5}	0.0110	0.0025
L(0,4)	2	5845.90	0.0014	2.8549×10^{-4}	5.7720×10^{-6}	0.0043	3.3196×10^{-4}
F(1,1)	2	2912.34	0.0016	3.5434×10^{-4}	1.5451×10^{-5}	0.0047	9.1307×10^{-4}
F(1,5)	2	5103.56	0.0047	7.7035×10^{-4}	1.5441×10^{-5}	0.0100	0.0054
F(1,6)	2	5864.83	0.0014	2.8804×10^{-4}	5.8241×10^{-6}	0.0043	3.4168×10^{-4}
F(1,7)	2	5403.87	0.0078	8.1188×10^{-4}	1.8269×10^{-5}	0.0171	8.0496×10^{-5}
T(0,3)	2	5385.32	0.0078	8.0536×10^{-4}	1.8147×10^{-5}	0.0197	4.2228×10^{-4}

elements. As it would be expected, the numerical errors of all modes, computed by SAFE or by SAIGA methods, decrease when N_{dof} increases. At low frequency ($f = 0.2$ MHz), the SAFE results of modes L(0,1) and F(1,1) have good precision when $N_{dof} = 504$, and the errors significantly decrease when $N_{dof} = 1080$. The precision of SAIGA solutions is even better: for example, the error of L(0,1) obtained by SAIGA with $N_{dof} = 360$ is smaller than the one obtained by SAFE with $N_{dof} = 1080$. At high frequency ($f = 2$ MHz), the h-convergence is achieved much faster when using SAIGA. The errors of SAIGA solution are typically about hundreds of times smaller than the SAFE's ones based on the same N_{dof}. Using SAIGA method with $N_{dof} = 504$ leads to similar precision than the one computed by using SAFE with $N_{dof} = 1080$.

In Fig. 4, we present the mode shapes of displacements computed for the mode L(0,1) at the frequency of 2 MHz. To be able to compare to the analytical solution which is derived in cylindrical coordinates system, the normalized displacement components U_r (radial), U_θ (circumferential), U_3 (longitudinal) along the thickness's direction are determined from the eigenvectors $\mathbf{U}$ (see Appendix B). The graphs show that the mode shapes obtained by the proposed SAIGA approach are in very good agreement with the exact solutions. It can also be checked that the SAIGA's solutions of circumferential displacement U_θ have vanished over the cylinder's section, which is consistent with our expectation for a longitudinal mode L(0,1) (Eq. (B.3)). By using the SAFE method with the same numerical parameters ($p = 3$, $N_{dof} = 1080$), the differences between numerical and exact solutions of mode shapes are visibly much more important. In particular, one may see that the U_θ components estimated by SAFE method are not zeros along the thickness's direction, which does not give a good representation of the axisymmetric feature of the considered mode L(0,1). Though, a good precision of the phase velocity computed by the SAFE method using the same numerical parameters has been achieved (error $= 9.0892 \times 10^{-4}$, see Table 2). Note that in this example, in comparison to the SAIGA method, using SAFE method disposes of some disadvantages due not only to the interpolation function but also to the description of the geometry.

To further investigate the efficiency of the proposed SAIGA formulation, we focus on some specific points in the dispersion curves of the phase velocity (C_{ph}). Fig. 5(a) depicts the numerical errors of C_{ph} of the mode L(0,1) at $f = 2$ MHz with respect to the total number of DOFs, which are computed by using Lagrange or NURBS basis functions with different orders (p). Conformity to the results presented in Table 2, it may be checked that the error obtained by employing SAIGA method is much smaller than the one obtained by the conventional SAFE method which has the same p and N_{dof}. Using NURBS-based basis function, even with low order ($p = 2, 3$), is shown to significantly improve the precision of C_{ph}'s numerical results. Moreover, convergence rates of the SAIGA solutions are much faster than SAFE's ones, especially when using high-order basis functions, i.e $p = 6$. Fig. 5(b) shows the k-refinement (increasing the polynomial order and then inserts knots (or elements)) of NURBS and Lagrange basis function at $N_{dof} = 1080$ and $N_{dof} = 1872$. It is shown that by increasing the order of basis function p, which increase the continuity of the NURBS basis function across the span, the global slope of the convergence curve of SAIGA's results is higher than SAFE's one.
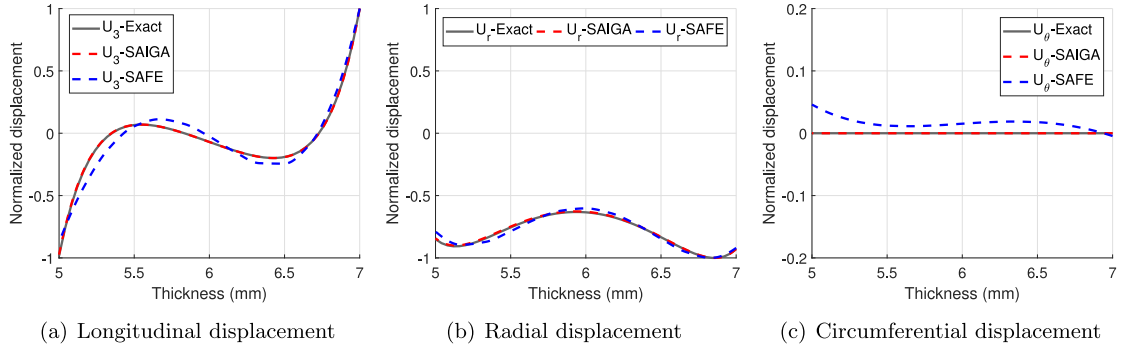
(a) Longitudinal displacement   (b) Radial displacement   (c) Circumferential displacement

Fig. 4. Mode shape of the mode L(0,1) at $f = 2$ MHz of a steel hollow cylinder: comparison between SAIGA solution (red dashed line), SAFE solution (blue dashed line) and analytical solution (gray line); both SAIGA and SAFE solutions are computed with $p = 3$, $N_{\mathrm{dof}} = 1080$. (For interpretation of the references to color in this figure legend, the reader is referred to the web version of this article.)
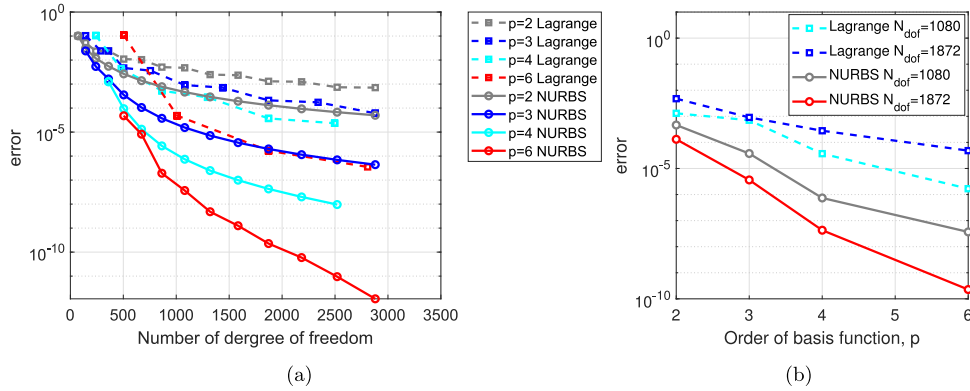

(a)   (b)

Fig. 5. Case of a homogeneous hollow cylinder: (a) relative error of the phase velocity of the mode L(0,1) at $f = 2$ MHz (b) k-refinement at the $N_{\mathrm{dof}} = 1080$ and $N_{\mathrm{dof}} = 1080$.

(a) SAIGA (N_{dof}=232)   (b) SAIGA (N_{dof}=329)   (c) SAIGA (N_{dof}=553)
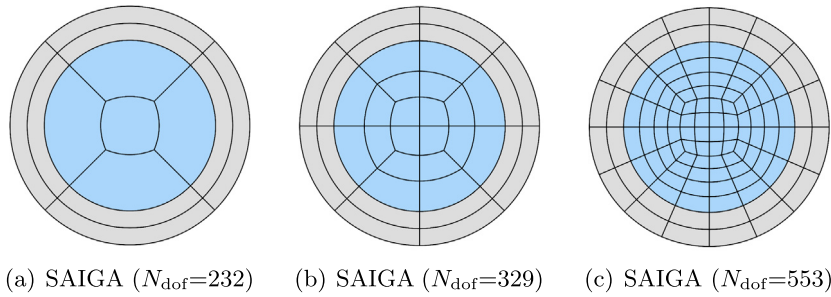
Fig. 6. Mesh discretization of a fluid-filled cylinder using NURBS and Lagrange basis functions of order $p = 3$.

4.2. Dispersion of guided-waves in fluid-filled cylinder

Guided-wave propagation in a steel cylinder filled by water, as shown in Fig. 2(b), is considered in this example. The steel cylinder has the same geometry and material properties as the one studied in the previous section. The acoustic properties of water are given by the density $\rho_1^f = 998$ kg m^{-3} and the sound speed $c_1^f = 1478$ m s^{-1}. The outer surface of the cylinder is assumed to be free.

Fig. 6 depicts illustrations of meshes used for simulations using SAIGA approach. For the geometrical description using IGA, four patches are used for the solid domain and five patches are used for the fluid's one (Fig. 6(a), (b),
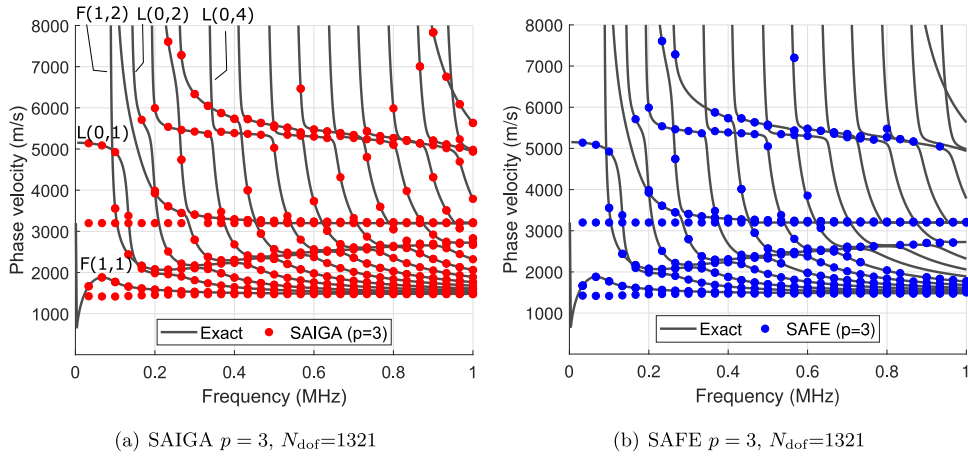
(a) SAIGA $p = 3$, $N_{\text{dof}} = 1321$ (b) SAFE $p = 3$, $N_{\text{dof}} = 1321$

Fig. 7. Dispersion curves of a fluid-filled steel cylinder: comparison between the analytical solution (gray line) and: (a) SAIGA solution (red marker), (b) SAFE solution (blue marker). (For interpretation of the references to color in this figure legend, the reader is referred to the web version of this article.)

Table 3
Case of a fluid-filled cylinder: error analysis based on h-refinement of SAIGA and SAFE ($p = 3$).

Mode	f (MHz)	$C_{\text{ph}}^{\text{Exact}}$ (m s^{-1})	err$^{\text{SAIGA}}$ $N_{\text{dof}} = 329$	err$^{\text{SAIGA}}$ $N_{\text{dof}} = 553$	err$^{\text{SAFE}}$ $N_{\text{dof}} = 616$	err$^{\text{SAFE}}$ $N_{\text{dof}} = 1321$
L(0,1)	0.2	1983.24	6.4898×10^{-6}	6.3073×10^{-6}	5.7993×10^{-5}	2.542×10^{-6}
L(0,1)	2	1584.89	2.7430×10^{-4}	4.484077×10^{-6}	1.6472×10^{-4}	5.2118×10^{-5}
L(0,2)	0.2	3986.96	1.6823×10^{-4}	3.5105×10^{-6}	0.0076	8.8835×10^{-5}
L(0,2)	2	1497.71	1.2490×10^{-4}	1.0421×10^{-4}	0.0042	7.2485×10^{-5}
L(0,4)	2	1567.14	0.00753	5.2335×10^{-4}	–	0.0016
F(1,1)	0.2	1584.89	1.0500×10^{-5}	4.4841×10^{-6}	1.3547×10^{-5}	3.4830×10^{-5}
F(1,1)	2	1478.05	1.9460×10^{-4}	1.9460×10^{-4}	9.1997×10^{-5}	1.2939×10^{-4}
F(1,2)	0.2	2078.20	5.0153×10^{-5}	7.0398×10^{-6}	3.0751×10^{-4}	3.2647×10^{-6}
F(1,2)	2	1488.92	1.0684×10^{-4}	1.0433×10^{-4}	3.1601×10^{-4}	5.7643×10^{-5}

(c)). It is worth noting that the fluid domain cannot be meshed by using one single patch because it leads to the singularity of the stress due to the collinearity of the control points. For the SAFE modeling, both fluid and solid domains are meshed by using quadrilateral elements.

We first validate the proposed FE formulations for calculating C_{ph}'s dispersion curves. Thanks to the simple cylindrical geometry, the considered fluid-filled hollow cylinder can also be solved by using the semi-analytical method [41] which was implemented in the Disperse software [40]. Note that when analyzing a coupled fluid–solid system, solving the dispersion equation may sometimes have numerical issues due to singularities when establishing transfer matrices. For this example, DISPERSE software starts to have difficulties to compute analytical solutions at frequencies higher than 1 MHz, and consequently, some modes are missed. On the contrary, using the finite element method, which requires higher computational costs, allows to avoid this kind of difficulty.

In Fig. 7, we compare the numerical solutions of C_{ph} obtained by SAIGA or SAFE methods to the analytical ones over the frequency range from 0 to 1 MHz. The discretization is performed by using cubic NURBS or Lagrange basis functions, respectively. The total number of degrees of freedom for both models equals $N_{\text{dof}} = 1321$. A similar filtering procedure as presented in the previous section was applied to extract the modes of interest according to their symmetries. It is shown that the dispersion curves computed by both SAIGA and SAFE methods agree well with the analytical dispersion ones. However, at high frequencies, some of the modes obtained from SAFE solutions could not be identified due to imprecise computed shape modes.

To quantify the accuracy SAIGA and SAFE methods in guided wave dispersion analysis, the relative errors of the phase velocity are investigated (Eq. (25)) at two frequencies of 0.2 MHz and 2 MHz. Similar to the previous study on the free hollow cylinder, we perform a h-refinement when fixing the basis function to be of order 3. Table 3 shows
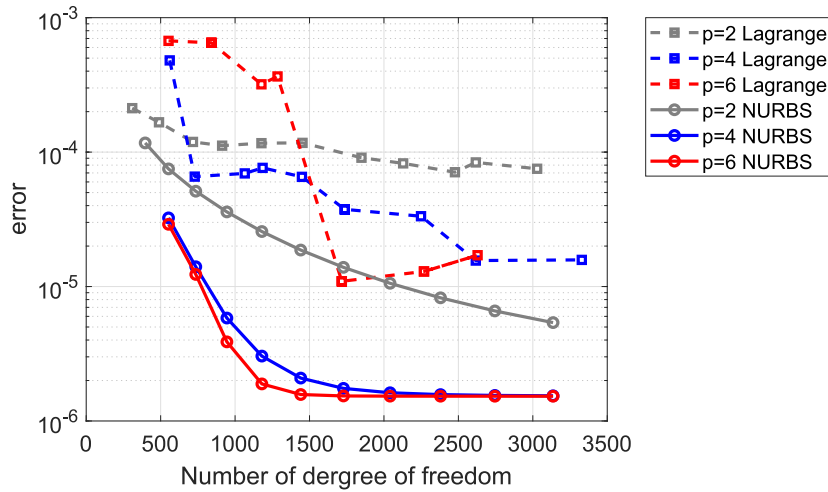
Fig. 8. Case of a fluid-filled cylinder: relative error of the phase velocity of the mode L(0,1) at $f = 2$ MHz.
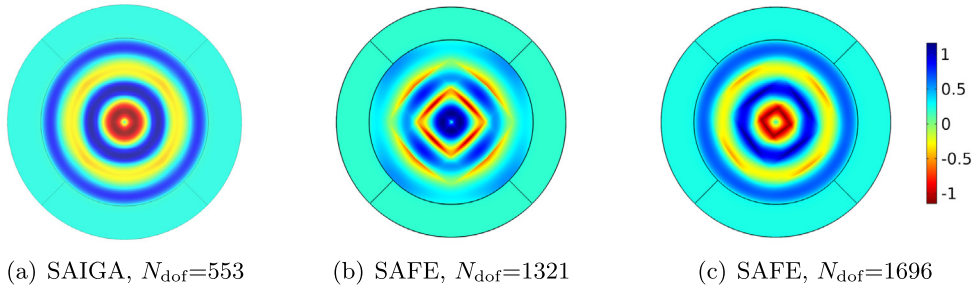

(a) SAIGA, $N_{\mathrm{dof}}=553$ (b) SAFE, $N_{\mathrm{dof}}=1321$ (c) SAFE, $N_{\mathrm{dof}}=1696$

Fig. 9. Displacement U_r mode shape for L(0,4) at the frequency $f = 2$ MHz (a) SAIGA with $p = 3$, $N_{\mathrm{dof}} = 553$, (b) SAFE with $p = 3$, $N_{\mathrm{dof}} = 1321$ and (b) SAFE with $p = 3$, $N_{\mathrm{dof}} = 1696$. (For interpretation of the references to color in this figure legend, the reader is referred to the web version of this article.)

that the SAIGA solutions using $N_{\mathrm{dof}} = 329$ or $N_{\mathrm{dof}} = 553$ have negligible errors at both low and high frequencies. On the contrary, by employing the conventional SAFE approach with $N_{\mathrm{dof}} = 616$ or $N_{\mathrm{dof}} = 1321$, which are much bigger than the ones used for SAIGA, the errors have greater values at both low and high frequencies. The results of a convergence analysis of C_{ph} of the mode L(0,1) at $f = 2$ MHz, in which SAFE and SAIGA methods are employed by using different orders of basis functions ($p = 2, 4, 6$), are presented in Fig. 8. It is shown that by using the same basis function order p, the global slope of the convergence curve of SAFE's results is much lower than SAIGA's one. Moreover, using higher-order basis functions in SAIGA allows to manifestly reduce the numerical errors. For the SAFE analysis, while the results using $p = 4$ clearly have better convergence than the ones obtained with $p = 2$, the advantage of using $p = 6$ is not clearly found in this example. Note that the asymptotic behavior of the errors when the becomes smaller than 10^{-6} is due to inaccurate reference solution, which was calculated using the Disperse software. In fact, although the Disperse's solutions were computed by using an analytical method, the results were exported in a format with limited digits after decimal point.

Fig. 9 presents the displacement shapes of the mode (L(0,4)) at high frequency $f = 2$ MHz. As the eigenvectors of the fluid domain derived from (Eq. (23)) are defined in terms of pressures, the fluid displacements shape modes may be determined using Euler's equation: $\boldsymbol{u}^f = -\frac{1}{\omega^2}\nabla p$. In this figure, the color isovalue surface represents the radial displacement component U_r of particles in both fluid and solid domains which are expected to be axisymmetric. Moreover, the radial displacements at the solid–fluid interface should theoretically be continuous to verify the interface condition (Eq. (4)). The SAIGA solution of U_r field, computed with $N_{\mathrm{dof}} = 553$ and has a C_{ph}'s error of 0.052% (see Table 3), is shown to be axisymmetric and continuous in agreeing with mentioned conditions. However, the solution of U_r in the fluid domain computed by SAFE method with $N_{\mathrm{dof}} = 1321$ is unlikely
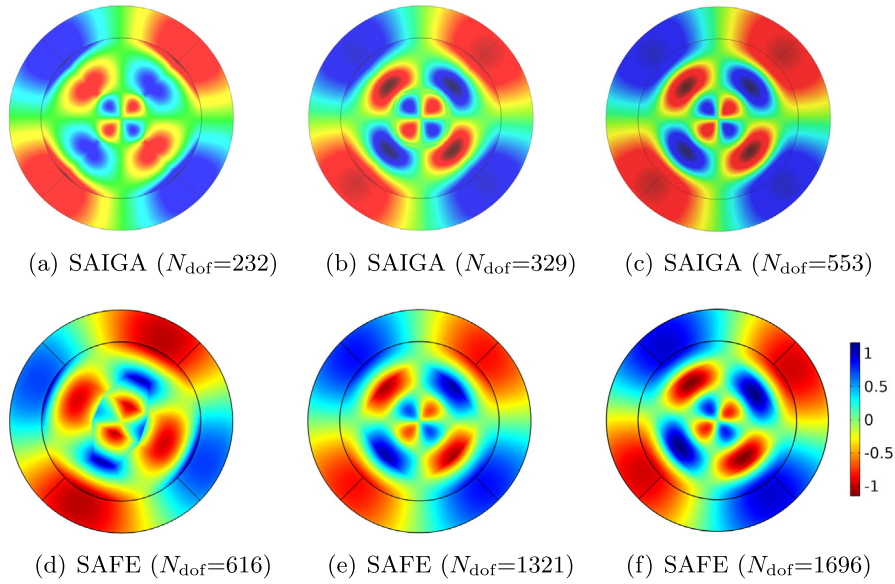
(a) SAIGA (N_{dof}=232)   (b) SAIGA (N_{dof}=329)   (c) SAIGA (N_{dof}=553)

(d) SAFE (N_{dof}=616)   (e) SAFE (N_{dof}=1321)   (f) SAFE (N_{dof}=1696)

Fig. 10. Displacement mode shape (U_r) of a flexural mode (F(2,2)) at low frequency ($f = 0.5$ MHz) and $C_{\text{ph}} = 2452.5$ m/s: (a, b, c) SAIGA with $p = 3$; (d, e, f) SAFE with $p = 3$.

axisymmetric (Fig. 9(b)), despite the fact that a correct solution of C_{ph} has been found (Table 3). Moreover, the fluid's radial displacements, computed by deriving the pressure solutions, do not conform to tho the solid's ones at the solid–fluid interface. The expected axisymmetry and continuity can be found by refining the FE mesh as shown in Fig. 9(c), requiring $N_{\text{dof}} = 1696$ which is about three times more than the number of DOFs required by SAIGA method ($N_{\text{dof}} = 553$). Using SAIGA has a greater advantage in this coupled problem thanks to the higher continuity of NURBS basis functions across the elements.

To further investigate the robustness of using SAIGA for mode shape calculation, in Fig. 10, we present the results of a higher-order mode (F(2,2)) at $f = 0.5$ MHz, computed by using SAIGA and SAFE approaches with different discretizations as plotted in Fig. 6. The isovalue surface represents the radial displacement in the solid or fluid domains. Again, the displacement fields in the fluid domain, which are derived from the pressure eigenvector, can be found to be more smooth when using SAIGA, even with much fewer elements. The mode shape obtained by using SAIGA with $N_{\text{dof}} = 329$ seems to have better quality than the one obtained by using SAFE with $N_{\text{dof}} = 1321$. Fig. 11 depicts the variation of the radial displacement components U_r of both fluid and solid phases along the solid–fluid interface. It can be checked that while fluid and solid solutions using SAIGA are perfectly matched from each to other (Fig. 11(b)), significant discontinuities are obtained when the SAFE method is used (Fig. 11(b)). Note that the errors of the phase velocity evaluated with SAIGA and SAFE methods are 3.297×10^{-5} and 8.867×10^{-5}, respectively.

4.3. Dispersion of guided-waves in a hollow cylinder immersed in fluid

Let us consider a water-filled steel cylinder immersed in an infinite water domain (Fig. 2(c)), which has been considered in numerous works [42] to investigate a numerical solution of leaky wave propagation in fluid immersed structures. The material properties of the steel cylinder and of the water are the same as the ones presented in the previous section. The infinite water domain is described by introducing a Perfectly Matched Layer (PML) as described in Section 2.2. The PML functions in the simulation are chosen as $\gamma_1 = \gamma_2 = 3 + 12i$ as given in [16]. The minimum thicknesses of the PMLs can be based on Eq. (10), which allows us to choose $h_1^{\text{pml}} = h_2^{\text{pml}} = 3.5$ mm for both PML domains in $\mathbf{e}_1$ and $\mathbf{e}_2$ directions.

We first perform a validation of the proposed FE formulations for calculating the dispersion curves of the phase of the considered fluid-filled and immersed cylinder within the frequency range $f = 0$-1 MHz. In Fig. 12, we compare
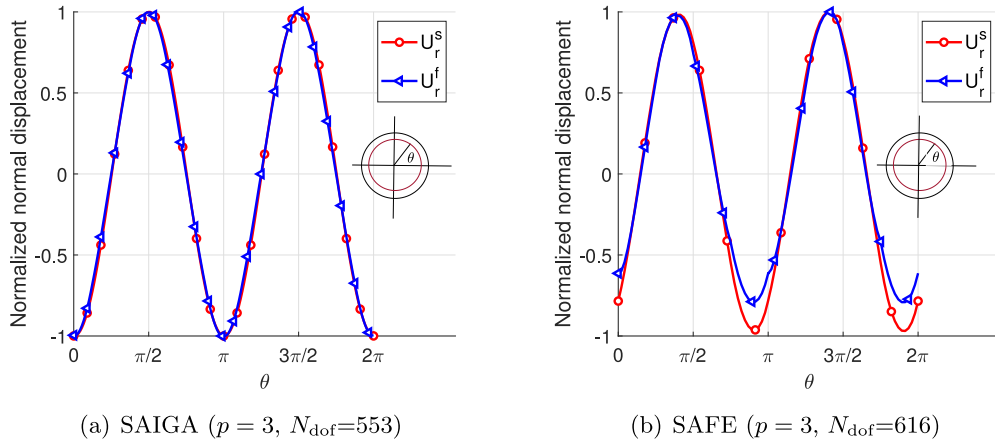
(a) SAIGA ($p = 3$, N_{dof}=553)　　　　(b) SAFE ($p = 3$, N_{dof}=616)

Fig. 11. Continuity of displacement for the solid–fluid interfaces of flexural mode (F(2,2)) U_r^s (solid domain) and U_r^f (fluid domain) of fluid-filled cylinder (a) SAIGA solution (b) SAFE solution.
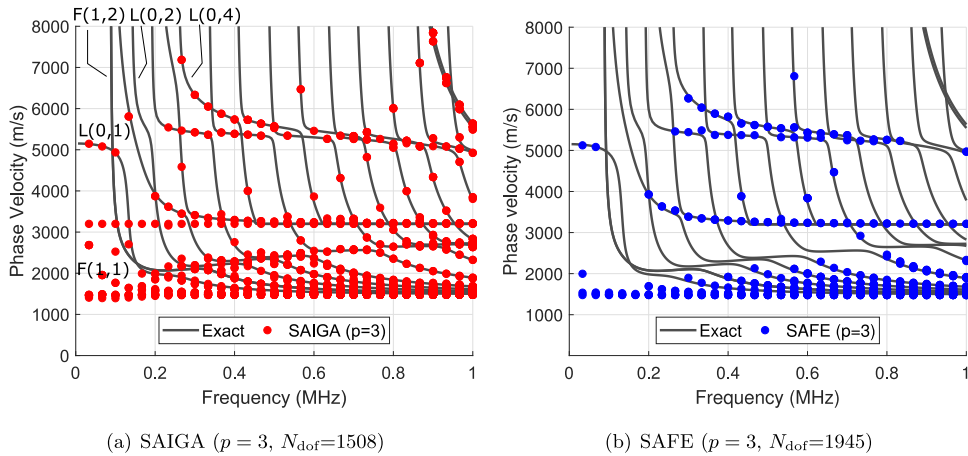

(a) SAIGA ($p = 3$, N_{dof}=1508)　　　　(b) SAFE ($p = 3$, N_{dof}=1945)

Fig. 12. Dispersion curves of a fluid-filled and immersed steel cylinder: comparison between (a) SAIGA solution (red marker), (b) SAFE solution (blue marker) and analytical solution (gray line). (For interpretation of the references to color in this figure legend, the reader is referred to the web version of this article.)

the analytical solutions of the phase velocities over the frequency range from 0 to 1 MHz with the numerical ones obtained by SAIGA and SAFE methods. The discretization is performed by using cubic NURBS basis functions. The total number of degrees of freedom required for the SAIGA and for SAFE is equal to $N_{\mathrm{dof}} = 1508$ and $N_{\mathrm{dof}} = 1945$, respectively. A similar filtering procedure as presented in the previous section has been applied to extract the modes of interest according to their symmetries. It is shown that the dispersion curves obtained from the proposed approach agree well with the analytical dispersion curves.

　　Mode shapes in terms of radial displacements are presented in Fig. 13. One may observe that leaky waves are totally damped in a very short distance when they go into the PML. It has been numerically checked with several larger domains (data not shown) that the solutions of interests do not depend on the location of the PMLs, showing the PML could efficiently attenuate leaky waves. As discussed previously, the displacement field in the fluid domains simulated by using the conventional SAFE method may have some discontinuities, as shown *e.g* in Fig. 13b ($N_{\mathrm{dof}} = 1945$), due to the smoothness drawback of the Lagrange polynomials. Consequently, the FE mesh should be extensively refined to obtain an accurate calculation of differentiation operators (Fig. 13c with $N_{\mathrm{dof}} = 9001$). Using SAIGA approach allows significantly to improve the smoothness of fluid's displacement with much fewer elements (Fig. 13a with $N_{\mathrm{dof}} = 1508$) thanks to the higher continuity of NURBS basis functions across
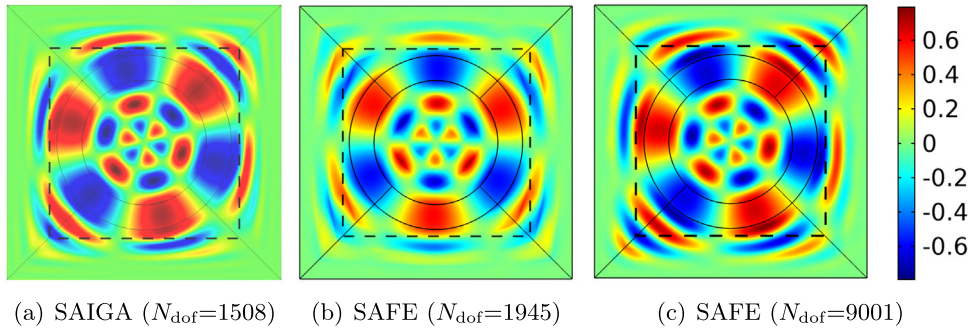
(a) SAIGA (N_{dof}=1508)   (b) SAFE (N_{dof}=1945)   (c) SAFE (N_{dof}=9001)

Fig. 13. Displacement U_r shape for a flexural mode (F(3,3)) at the frequency of $f = 0.5$ MHz and $C_{\mathrm{ph}} = 3791$ m/s (a) SAIGA with $p = 3$, $N_{\mathrm{dof}} = 1508$ (b) SAFE with $p = 3$, $N_{\mathrm{dof}} = 1945$ (b) SAFE with $p = 3$, $N_{\mathrm{dof}} = 9001$.

the elements. Moreover, the conventional SAFE approach suffers from a non-smoothness profile across the PML interfaces, which leads to imperfect absorption of the leaky modes. Using NURBS leads to better continuity of solid and fluid normal displacements at the interface, and consequently, it would be preferable to use higher-order NURBS basis functions for modeling leaky wave in fluid–solid coupled systems.

4.4. Anisotropic waveguide with arbitrary cross-section coupling with fluids

As a final example, we demonstrate the merits of using SAIGA in the analysis of guided wave propagation in a more complex geometry structure. Let us consider a waveguide representing a long cortical bone with real cross-section, which has been reported by many authors using the conventional SAFE method in the literature [13,43]. The domain of interests consists of one transversely isotropic elastic solid sandwiched between two homogeneous fluid domains, which represents the cortical bone, the marrow (inner fluid) and the soft tissue (outer fluid), respectively. The cortical has a mean thickness of 7 mm . The inner fluid (bone marrow) has approximately 15 mm-diameter and the outer fluid (soft tissue) has a thickness of 3 mm-thickness (Fig. 2(d)) [44]. The mass density of the cortical bone is given by $\rho = 1722$ kg m^{-3}. The non-zero entries of the elasticity tensor are taken as: $C_{11} = C_{22} = 15.1$ GPa, $C_{13} = C_{23} = 8.7$ GPa, $C_{33} = 23.5$ GPa, $C_{44} = C_{55} = 4.7$ GPa and $C_{66} = 3.3$ GPa [14]. The bone marrow and soft tissue were modeled as homogeneous idealized acoustic fluids. The bone marrow is characterized with the density $\rho_1^f = 930$ kg m^{-3} and sound speed $c_1^f = 1480$ m s^{-1}, while the characteristics of soft tissue are given by the density $\rho_2^f = 1043$ kg m^{-3} and sound speed $c_2^f = 1561$ m s^{-1} [13].

The geometry is built from 13 patches including four patches for the outer fluid domain, four patches for the bone's section and five patches for the inner fluid domain. Thus, we have several interfaces with C^0-continuity between the patches and C^{p-k}-continuity between the elements within the patches, which is a useful feature in the majority of practical applications. The NURBS geometries and positions of control points for these three domains are depicted in Fig. 14(a, b, c).

As the analytical solution does not exist for this coupled system, the validation of SAIGA method was performed by comparing to SAFE solution. Fig. 15 depicts the fine FE mesh of cubic Lagrangian elements ($N_{\mathrm{dof}} = 12929$) used to obtain a "reference" solution. We also present in Fig. 15a and b two NURBS-based meshes which are built with cubic and eight-order NURBS basis functions, respectively. Note that the numbers of DOFs associated to these meshes are nearly equal, which are $N_{\mathrm{dof}} = 2683$ and $N_{\mathrm{dof}} = 2689$, respectively. As NURBS allows to represent exact curvature of this geometry, the SAIGA meshes shown in Fig. 15b, c require less number of elements and are much more regular than the FE mesh with triangular elements (Fig. 15a) which requires fine refinement at high curvature zones. When using $p = 8$, only one element is needed for each patch.

Fig. 16 presents the dispersion curves of phase velocity in the frequency range 0–100 kHz, computed by using SAFE and SAIGA methods. The SAIGA solutions were computed with $p = 3$, $p = 6$, $p = 8$ and $p = 10$. Similar to the examples previously presented, using SAIGA with all orders $p = 3, 6, 8, 10$ allows to capture very well the reference solution at low frequencies. Fig. 17(a, b, c) depict the mode shape in terms of the radial displacement computed by using SAIGA method with ($p = 3$ or $p = 8$) or using SAFE method ($p = 3$) with very fine
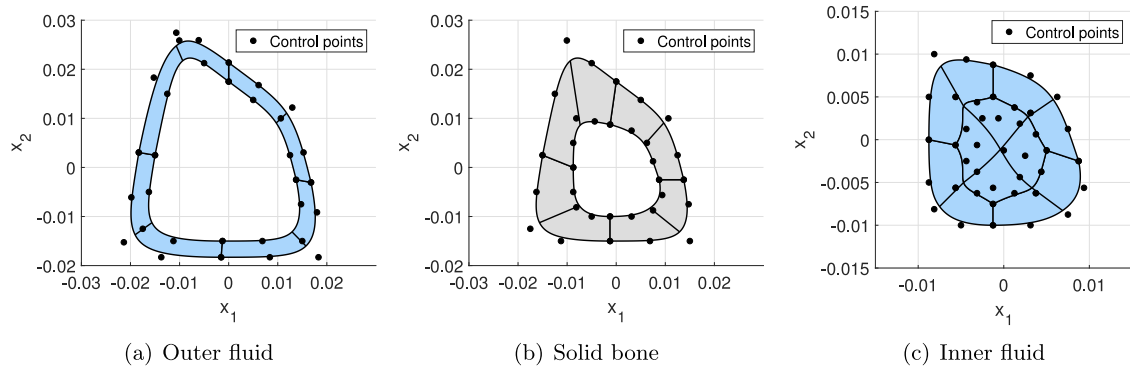
(a) Outer fluid   (b) Solid bone   (c) Inner fluid

Fig. 14. Geometry illustration and position of control points created from NURBS of $p = 3$ for (a) outer soft tissue (b) core of cortical bone and (c) inner bone marrow.
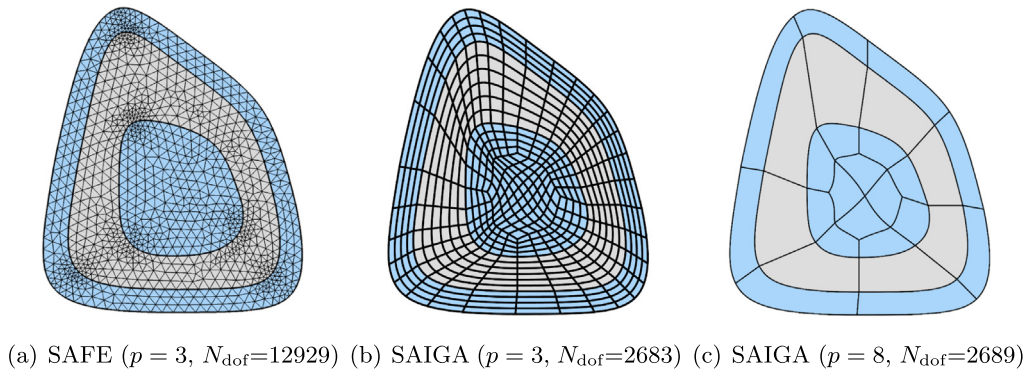

(a) SAFE ($p = 3$, N_{dof}=12929) (b) SAIGA ($p = 3$, N_{dof}=2683) (c) SAIGA ($p = 8$, N_{dof}=2689)

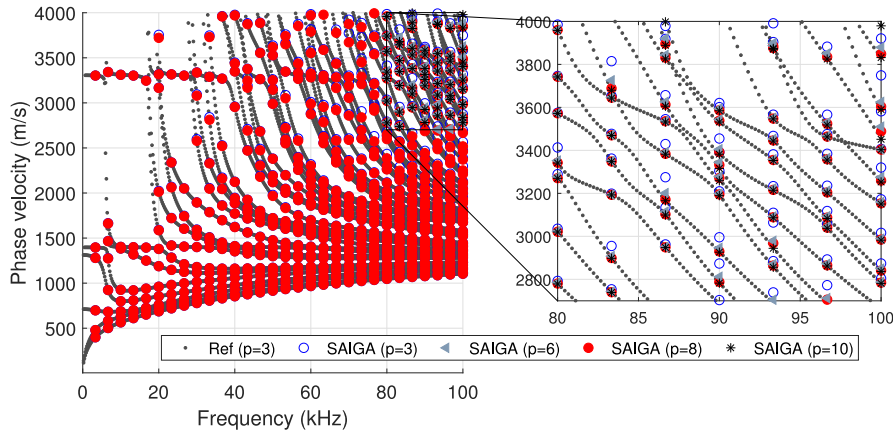**Fig. 15.** Meshes of a bone's section coupled with marrow and soft tissue.

Fig. 16. Phase velocity *versus* frequency in a coupled soft tissue-cortical bone system: comparison between the reference SAFE solution (gray marker, $p = 3$, $N_{\mathrm{dof}} = 12929$) and SAIGA solutions (blue marker: $p = 3$, $N_{\mathrm{dof}} = 2689$; gray marker: $p = 6$, $N_{\mathrm{dof}} = 2683$; gray marker: $p = 6$, $N_{\mathrm{dof}} = 2689$; black marker: $p = 10$, $N_{\mathrm{dof}} = 4249$). (For interpretation of the references to color in this figure legend, the reader is referred to the web version of this article.)

discretization. The presented mode is found at $f = 50$ KHz and $C_{\mathrm{ph}} = 1160$ m/s. It may be observed that SAIGA results of the considered mode shape, which are computed by using $p = 3$ and $p = 8$ and have almost the same N_{dof}, have both good agreements with the reference solution.

(a) SAIGA ($p = 3$, N_{dof}=2683)   (b) SAIGA ($p = 8$, N_{dof}=2689)   (c) SAFE ($p = 3$, N_{dof}=12929)
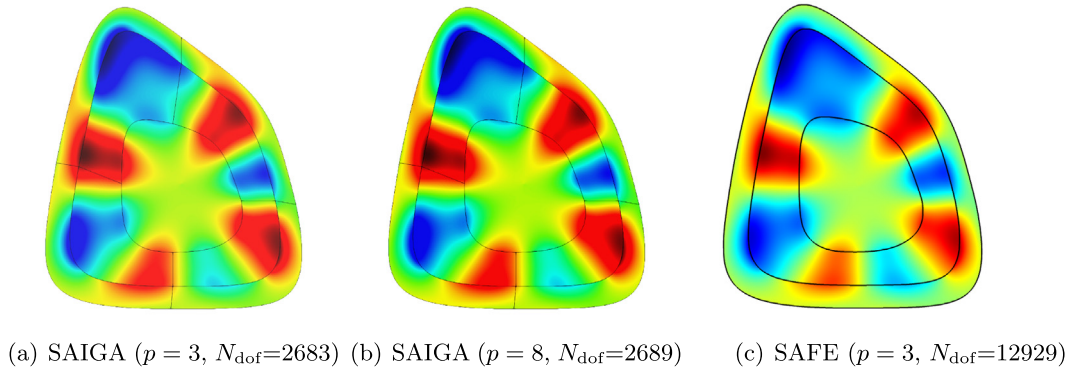
Fig. 17. Displacement U_r of flexural mode at the $f = 50$ kHz and $C_{\text{ph}} = 1160$ m/s for the cortical bone coupled with the bone marrow and the soft tissue (a) SAIGA with $p = 3$, $N_{\text{dof}} = 2683$, (b) SAIGA with $p = 8$, $N_{\text{dof}} = 2689$ and (c) SAFE with $p = 3$, $N_{\text{dof}} = 12929$.

The calculation of higher-order modes at high frequency requires more refinement. Hence, we focus to examine the solutions of the phase velocity in a zoomed window as shown in Fig. 16. It is clearly seen that the difference between SAIGA solution with $p = 3$ and the reference ones is significant. The solutions with $p = 6$ are better, yet they still do not match well with the reference values at some locations. The solutions obtained with $p = 8$ and $p = 10$ are perfectly in agreement with reference ones, showing that the convergence is archived. Note that while the N_{dof} of the cases $p = 3, 6, 8$ are quite similar (about 2600 DOFs), using $p = 10$ requires a greater value of N_{dof} ($N_{\text{dof}} = 4249$). Therefore, employing NURBS with $p = 8$, for which only one element per patch is needed, would be the best choice for this example for calculating the phase velocities.

In Fig. 18, we investigated the continuity of solid and fluid displacements at the interfaces of a mode at $f = 100$ kHz. To do so, the solid and fluid displacement components, which are normal to the fluid–solid interfaces, are compared. It is worth noting that the SAFE's mesh used for the simulation has a similar N_{dof} to the SAIGA's one, in which each patch is modeled by only one eight-order NURBS element. It was shown that while fluid–solid displacement's continuity condition may be precisely satisfied by using SAIGA's results, SAFE's solution suffers from significant errors at both interior and exterior interfaces. Furthermore, the errors of the fluid's displacement seemed to be more significant than the solid's ones. This would be due to the numerical errors of the fluid pressure's gradient estimation. This comparison confirms again the advantage of using NURBS for studying the mode shapes in coupled fluid–solid system.

5. Conclusion

In this paper, a semi-analytical isogeometric analysis (SAIGA) for the anisotropic elastic waveguides coupled with fluid was proposed to improve the efficiency of guided wave modeling in comparison with the conventional SAFE method. The convergence analysis for isotropic homogeneous hollow cylinder and fluid-filled cylinder showed that increasing the order of NURBS basis function yields a much faster convergence rate in comparison with a similar process using Lagrange polynomials. When considering elastic waveguides coupled with fluids, using NURBS basis functions can significantly improve the evaluation of not only dispersed wavenumbers but also mode shapes. In particular, using SAIGA allows to obtain excellent continuity at the solid–fluid interface, which is much more difficult to achieve when using conventional SAFE. Moreover, it has been shown that waveguides immersed in an infinite fluid may efficiently be modeled by introducing perfectly matched layers (PML) and then employing SAIGA procedure.

In terms of computational time, our numerical experiences showed that using SAGA allows to reduce significantly the computational time to archive a similar precision. It was also observed that using the same number of DOFs, SAFE and SAIGA required similar computational times. However, a rigorous comparison of computational times requires that both methods should be implemented in a same environment. Note that in this work, while the SAFE simulation was performed in Comsol Multiphysics, the SAIGA method was implemented in an in-house Matlab code.
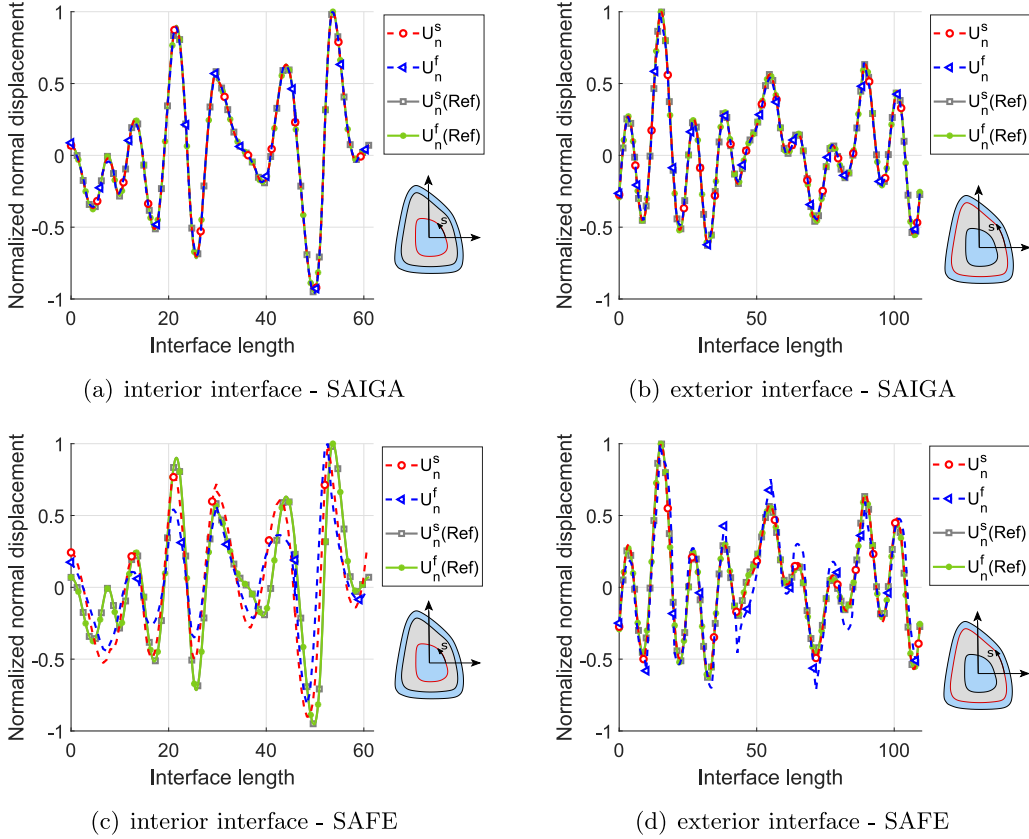
Fig. 18. Continuity of displacement at the bone–soft tissue interfaces of a flexural mode at the $f = 100$ kHz and $C_{\mathrm{ph}} = 3980$ m/s : U_n^s (solid domain) and U_n^f (fluid domain) (a, b) SAIGA solution ($p = 8$, $N_{\mathrm{dof}} = 2689$); (c, d) SAFE solution ($p = 3$, $N_{\mathrm{dof}} = 2675$).

For wave propagation simulation using FEM, it is well-known that the discretization needs to ensure a number of elements which is sufficient not only for simulating interested wavelengths, but also for correctly describing the curved boundaries. The advantage of SAIGA in this context, besides its better continuity feature as mentioned before, is that using NURBS allows to represent exact curvature, hence it does not require as much number of elements as the one required by the conventional SAFE method for describing the curved interface between fluid and solid domains. The proposed SAIGA procedure was shown to be particularly interesting for studying arbitrary cross-section waveguides in terms of computational cost as well as of accuracy.

Extensions of the proposed SAIGA formulation may be developed for studying guided-wave propagation in poroelastic [45] or second-gradient media [46], for which the high-order continuity of NURBS would be interesting to improve the simulation efficiency.

Declaration of competing interest

The authors declare that they have no known competing financial interests or personal relationships that could have appeared to influence the work reported in this paper.

Appendix A. Equations in the frequency–wavenumber domain

Noting that in the frequency–wavenumber ($\omega - k_3$) domain, the time derivative and the spatial derivative with respect to x_1 can be replaced by: $(\dot{\star}) \rightarrow -\mathrm{i}\omega(\star)$ and $\partial_1(\star) \rightarrow \mathrm{i}k_3(\star)$, respectively, then the amplitudes of the strain and stress vectors ($\tilde{\boldsymbol{e}}$ and $\tilde{\boldsymbol{s}}$) are expressed by:

$$\tilde{\boldsymbol{e}} = (\mathbf{L}_1\partial_1 + \mathbf{L}_2\partial_2 + \mathrm{i}k_3\mathbf{L}_3)\tilde{\boldsymbol{u}}^s, \tag{A.1}$$

$$\tilde{\boldsymbol{s}} = \mathbf{C}\tilde{\boldsymbol{e}}, \tag{A.2}$$

and the balance equation (1) can be reformulated as a 2D system of equations with respect to (x_2, x_3):

$$-\rho\omega^2\tilde{\boldsymbol{u}}^s - \left(\mathbf{L}_1^T\partial_1 + \mathbf{L}_2^T\partial_2 + ik_3\mathbf{L}_3^T\right)\mathbf{C}(\mathbf{L}_1\partial_1 + \mathbf{L}_2\partial_2 + ik_3\mathbf{L}_3)\tilde{\boldsymbol{u}}^s = 0, \quad \forall\bar{\boldsymbol{x}} \in \bar{\Omega}^s. \tag{A.3}$$

Similarly, by substituting Eq. (11b) into Eq. (3), the wave equations in the fluid domains are simplified into a two-dimensional problem:

$$(-\rho_\alpha^f\omega^2 + k_3^2 K_\alpha^f)\tilde{p}_\alpha - K_\alpha^f(\partial_1^2 + \partial_2^2)\tilde{p}_\alpha = 0, \quad \forall\bar{\boldsymbol{x}} \in \bar{\Omega}_\alpha^f. \tag{A.4}$$

The boundary conditions in Eqs. (4)–(5) read:

$$\left.\begin{aligned} \tilde{\boldsymbol{u}}^s \cdot \mathbf{n}^s &= \frac{1}{\rho_\alpha^f\omega^2}(n_1\partial_1 + n_2\partial_2)\tilde{p}_\alpha \\ \tilde{\boldsymbol{t}} &= -\tilde{p}_\alpha\mathbf{n}^s \end{aligned}\right\} \quad \forall\tilde{\boldsymbol{x}} \in \bar{\Gamma}_\alpha^{sf}(\alpha = \{1, 2\}), \tag{A.5}$$

$$\tilde{p}_\alpha \to 0 \qquad \text{when } |\tilde{\boldsymbol{x}}| \to \infty, \tag{A.6}$$

where $\tilde{\boldsymbol{t}} = (n_1\mathbf{L}_1^T + n_2\mathbf{L}_2^T)\tilde{\boldsymbol{s}}$.

Appendix B. Mode filtering for cylindrical waveguides

In hollow cylinders, there exist several guided waves denoted by longitudinal modes $L(m, n)$, torsional modes $T(m, n)$ and flexural modes $F(m, n)$ where the integer m denotes the circumferential order of a mode and the integer n represents the group order of a mode [1]. The guided waves contain axisymmetric modes ($m = 0$) and non-axisymmetric modes (also known as flexural modes). A modal filtering must be processed to identify and separate two fundamental modes: axisymmetric longitudinal modes $L(0, n)$ and non-axisymmetric flexural modes $F(1, n)$. In order to apply a filtering criteria, the Cartesian displacement solution $\mathbf{U} = \{U_1, U_2, U_3\}^T$ must be converted into the cylindrical coordinates solution $\mathbf{U} = \{U_r, U_\theta, U_3\}^T$ as follows:

$$U_r = U_1\cos(\theta) + U_2\sin(\theta), \qquad U_\theta = -U_1\sin(\theta) + U_2\cos(\theta), \tag{B.1}$$

where $\theta = \arctan(\frac{x_2}{x_1})$. For modes with $m = 0$, the derivatives of the displacement components with respect to θ vanish [47]

$$\partial_\theta U_r = \partial_\theta U_\theta = \partial_\theta U_3 = 0, \tag{B.2}$$

additionally, the longitudinal modes have dominant particle motions in either the r and/or $\mathbf{e}_3$ direction, which means:

$$U_\theta = 0. \tag{B.3}$$

For modes with $m = 1$, the filtering criteria can be written as:

$$\partial_\theta U_r = \partial_\theta U_\theta \text{ and } \partial_\theta U_3 = 0 \tag{B.4}$$

References

[1] J.L. Rose, Ultrasonic Guided Waves in Solid Media, Cambridge University Press, 2014.
[2] A. Vaziri Astaneh, M.N. Guddati, Improved inversion algorithms for near-surface characterization, Geophys. J. Int. 206 (2) (2016) 1410–1423.
[3] X. Yu, Z. Fan, S. Puliyakote, M. Castaings, Remote monitoring of bond line defects between a composite panel and a stiffener using distributed piezoelectric sensors, Smart Mater. Struct. 27 (3) (2018) 035014.
[4] Z. Fan, M. Lowe, M. Castaings, C. Bacon, Torsional waves propagation along a waveguide of arbitrary cross section immersed in a perfect fluid, J. Acoust. Soc. Am. 124 (4) (2008) 2002–2010.
[5] D. Ta, W. Wang, Y. Wang, L.H. Le, Y. Zhou, Measurement of the dispersion and attenuation of cylindrical ultrasonic guided waves in long bone, Ultrasound Med. Biol. 35 (4) (2009) 641–652.
[6] T.N. Tran, M.D. Sacchi, D. Ta, V.-H. Nguyen, E. Lou, L.H. Le, Nonlinear inversion of ultrasonic dispersion curves for cortical bone thickness and elastic velocities, Ann. Biomed. Eng. 47 (11) (2019) 2178–2187.
[7] T. Falardeau, P. Belanger, Ultrasound tomography in bone mimicking phantoms: Simulations and experiments, J. Acoust. Soc. Am. 144 (5) (2018) 2937–2946.
[8] C. Baron, Propagation of elastic waves in an anisotropic functionally graded hollow cylinder in vacuum, Ultrasonics 51 (2) (2011) 123–130.
[9] K.-L. Nguyen, F. Treyssede, C. Hazard, Numerical modeling of three-dimensional open elastic waveguides combining semi-analytical finite element and perfectly matched layer methods, J. Sound Vib. 344 (2015) 158–178.

[10] W. Duan, R. Kirby, Guided wave propagation in buried and immersed fluid-filled pipes: Application of the semi analytic finite element method, Comput. Struct. 212 (2019) 236–247.

[11] M. Mazzotti, M. Miniaci, I. Bartoli, A numerical method for modeling ultrasonic guided waves in thin-walled waveguides coupled to fluids, Comput. Struct. 212 (2019) 248–256.

[12] P. Zuo, Z. Fan, Modal properties of elastic surface waves in the presence of material anisotropy and prestress, J. Sound Vib. 485 (2020) 115588.

[13] D. Pereira, G. Haiat, J. Fernandes, P. Belanger, Simulation of acoustic guided wave propagation in cortical bone using a semi-analytical finite element method, J. Acoust. Soc. Am. 141 (4) (2017) 2538–2547.

[14] V.-H. Nguyen, S. Naili, Ultrasonic wave propagation in viscoelastic cortical bone plate coupled with fluids: A spectral finite element study, Comput. Methods Biomech. Biomed. Eng. 16 (9) (2013) 963–974.

[15] M. Mazzotti, A. Marzani, I. Bartoli, Dispersion analysis of leaky guided waves in fluid-loaded waveguides of generic shape, Ultrasonics 54 (1) (2014) 408–418.

[16] P. Zuo, Z. Fan, SAFE–PML approach for modal study of waveguides with arbitrary cross sections immersed in inviscid fluid, J. Sound Vib. 406 (2017) 181–196.

[17] A.V. Astaneh, M.N. Guddati, Efficient computation of dispersion curves for multilayered waveguides and half-spaces, Comput. Methods Appl. Mech. Engrg. 300 (2016) 27–46.

[18] A.V. Astaneh, M.N. Guddati, Dispersion analysis of composite acousto-elastic waveguides, Composites B 130 (2017) 200–216.

[19] T. Hughes, J. Cottrell, Y. Bazilevs, Isogeometric analysis: CAD, finite elements, NURBS, exact geometry and mesh refinement, Comput. Methods Appl. Mech. Engrg. 194 (39) (2005) 4135–4195.

[20] T. Nguyen, T. Ngo, H. Nguyen-Xuan, A novel three-variable shear deformation plate formulation: theory and isogeometric implementation, Comput. Methods Appl. Mech. Engrg. 326 (2017) 376–401.

[21] T. Nguyen, C. Thai, T. Luu, H. Nguyen-Xuan, J. Lee, NURBS-Based postbuckling analysis of functionally graded carbon nanotube-reinforced composite shells, Comput. Methods Appl. Mech. Engrg. 347 (2019) 983–1003.

[22] J. Cottrell, A. Reali, Y. Bazilevs, T. Hughes, Isogeometric analysis of structural vibrations, Comput. Methods Appl. Mech. Engrg. 195 (41) (2006) 5257–5296.

[23] T.J. Hughes, J.A. Evans, A. Reali, Finite element and NURBS approximations of eigenvalue, boundary-value, and initial-value problems, Comput. Methods Appl. Mech. Engrg. 272 (2014) 290–320.

[24] T. Hughes, A. Reali, G. Sangalli, Duality and unified analysis of discrete approximations in structural dynamics and wave propagation: Comparison of p-method finite elements with k-method NURBS, Comput. Methods Appl. Mech. Engrg. 197 (49) (2008) 4104–4124.

[25] H. Gravenkamp, A.A. Saputra, S. Duczek, High-order shape functions in the scaled boundary finite element method revisited, Arch. Comput. Methods Eng. (2019) 1–22.

[26] C. Willberg, S. Duczek, J.V. Perez, D. Schmicker, U. Gabbert, Comparison of different higher order finite element schemes for the simulation of lamb waves, Comput. Methods Appl. Mech. Eng. 241 (2012) 246–261.

[27] H. Gravenkamp, S. Natarajan, W. Dornisch, On the use of NURBS-based discretizations in the scaled boundary finite element method for wave propagation problems, Comput. Methods Appl. Mech. Engrg. 315 (2017) 867–880.

[28] Y. Liu, Q. Han, Y. Liang, G. Xu, Numerical investigation of dispersive behaviors for helical thread waveguides using the semi-analytical isogeometric analysis method, Ultrasonics 83 (2018) 126–136.

[29] F. Seyfaddini, H. Nguyen-Xuan, V.-H. Nguyen, A semi-analytical isogeometric analysis for wave dispersion in functionally graded plates immersed in fluids, Acta Mech. 232 (2021) 15–32.

[30] C. Li, Q. Han, Y. Liu, Z. Wang, Wave isogeometric analysis method for calculating dispersive properties of guided waves in rotating damped cylinders, Meccanica 54 (1) (2019) 169–182.

[31] Y. Liu, S. Lin, Y. Li, C. Li, Y. Liang, Numerical investigation of Rayleigh waves in layered composite piezoelectric structures using the SIGA–PML approach, Composites B 158 (2019) 230–238.

[32] F. Teixeira, W.C. Chew, Complex space approach to perfectly matched layers: A review and some new developments, Int. J. Numer. Modelling, Electron. Netw. Devices Fields 13 (5) (2000) 441–455.

[33] H. Gravenkamp, C. Birk, C. Song, Numerical modeling of elastic waveguides coupled to infinite fluid media using exact boundary conditions, Comput. Struct. 141 (2014) 36–45.

[34] T. Hayashi, D. Inoue, Calculation of leaky lamb waves with a semi-analytical finite element method, Ultrasonics 54 (6) (2014) 1460–1469.

[35] T.J. Hughes, The Finite Element Method: Linear Static and Dynamic Finite Element Analysis, Courier Corporation, 2012.

[36] L. Piegl, W. Tiller, The NURBS Book, Springer Science & Business Media, 2012.

[37] J.A. Cottrell, T.J. Hughes, Y. Bazilevs, Isogeometric Analysis: Toward Integration of CAD and FEA, John Wiley & Sons, 2009.

[38] L. Dedè, C. Jäggli, A. Quarteroni, Isogeometric numerical dispersion analysis for two-dimensional elastic wave propagation, Comput. Methods Appl. Mech. Engrg. 284 (2015) 320–348.

[39] V.-H. Nguyen, T.N. Tran, M.D. Sacchi, S. Naili, L.H. Le, Computing dispersion curves of elastic/viscoelastic transversely-isotropic bone plates coupled with soft tissue and marrow using semi-analytical finite element (SAFE) method, Comput. Biol. Med. 87 (2017) 371–381.

[40] M. Lowe, B. Pavlakovic, Disperse Users manual, 2013.

[41] C. Aristegui, M. Lowe, P. Cawley, Guided waves in fluid-filled pipes surrounded by different fluids, Ultrasonics 39 (5) (2001) 367–375.

[42] M.K. Kalkowski, J.M. Muggleton, E. Rustighi, Axisymmetric semi-analytical finite elements for modelling waves in buried/submerged fluid-filled waveguides, Comput. Struct. 196 (2018) 327–340.

[43] T. Tran, L. Le, M. Sacchi, V.-H. Nguyen, Sensitivity analysis of ultrasonic guided waves propagating in trilayered bone models: A numerical study, Biomech. Model. Mechanobiol. 17 (2018) 1269?1279.

[44] J.H. Gosman, Z.R. Hubbell, C.N. Shaw, T.M. Ryan, Development of cortical bone geometry in the human femoral and tibial diaphysis, Anat. Rec. 296 (5) (2013) 774–787.

[45] V.-H. Nguyen, S. Naili, Simulation of ultrasonic wave propagation in anisotropic poroelastic bone plate using hybrid spectral/finite element method, Int. J. Numer. Methods Biomed. Eng. 28 (8) (2012) 861–876.

[46] A. Charalambopoulos, L.N. Gergidis, G. Kartalos, On the gradient elastic wave propagation in cylindrical waveguides with microstructure, Composites B 43 (6) (2012) 2613–2627.

[47] H. Gravenkamp, C. Birk, C. Song, The computation of dispersion relations for axisymmetric waveguides using the scaled boundary finite element method, Ultrasonics 54 (5) (2014) 1373–1385.